1 **Trace element perspective into the *ca*. 2.1-billion-year-old shallow-marine microbial**

2 **mats from the Francevillian Group, Gabon**

3

4 Jérémie Aubineau[1]*, Abderrazak El Albani[1], Andrey Bekker[2, 3], Ernest Chi Fru[4], Andrea

5 Somogyi[5], Kadda Medjoubi[5], Armelle Riboulleau[6], Alain Meunier[1], & Kurt O. Konhauser[7]

6

7 [1]UMR 7285 CNRS IC2MP, University of Poitiers, Poitiers, France

8 [2]Department of Earth and Planetary Sciences, University of California, Riverside, CA, 92521,

9 USA

10 [3]Department of Geology, University of Johannesburg, Auckland Park 2006, South Africa

11 [4]Centre of Geobiology and Geochemistry, School of Earth and Ocean Sciences, College of

12 Physical Sciences and Engineering, Cardiff University, Cardiff CF10 3AT, Wales, UK

13 [5]Nanoscopium beamline Synchrotron Soleil, BP 48, Saint-Aubin, 91192 GIF-sur-Yvette,

14 France

15 [6]UMR 8187 CNRS LOG, University of Lille, ULCO, Villeneuve d'Ascq, France.

16 [7]Department of Earth and Atmospheric Sciences, University of Alberta, Edmonton, Alberta,

17 Canada.

18

19 *corresponding author: jeremie.aubineau@univ-poitiers.fr

Abstract

The sedimentary fabrics of Precambrian mat-related structures (MRS) represent some of the oldest convincing evidence for early life on Earth. The *ca.* 2.1 billion-year (Ga) old MRS in the FB2 Member of the Francevillian basin in Gabon has received considerable attention not only because they contain remnants of microbial mats that colonized large areas in oxygenated, shallow-marine settings, but they also contain evidence for ancient multicellular organisms that thrived on these microbial mats using them as a food source. Despite these insights, what remains lacking is a full characterization of the geochemical composition of the MRS to test whether the bulk composition of fossilized MRS is distinct from the host sediments (sandstones and shales). Here, we show that the trace element (TE) content of microbial textures belonging to pyritized MRS, poorly pyritized MRS, and "elephant-skin" textures (EST) is highly variable and differs from that of the host sediments. The poorly pyritized MRS contain a unique matrix with embedded Ti- and Zr-rich minerals and syngenetically enriched in TE. The EST, some of which are developed along the same stratigraphic horizon as the poorly pyritized MRS, display a distinct distribution of TE-bearing heavy minerals, suggesting a local difference in physical conditions during sedimentation. Similarly, high chalcophile-element (CE) content in pyritized MRS relative to the host sediments of the FB2 Member further points to local bacterially influenced enrichments with high rates of microbial sulfate reduction during early diagenesis. The geochemical relationship between the MRS and the Francevillian sediments (*e.g.*, FB, FC, and FD formations) indicates that specific biological pathways for CE enrichments (*i.e.*, microbially controlled accumulation) are not apparent. Our findings highlight bulk-rock TE distinction between the 2.1-billion-year-old MRS and their host sediments, but also indicate that environmental conditions, such as hydrodynamic regime and water-column redox chemistry, may simply overwhelm any potential biological signal. Our data suggest that the microbial impact may have only passively influenced TE enrichment in the studied sediments, implying that TE concentrations in MRS are a poor biosignature. Importantly, this work indicates that bulk TE geochemistry does not unveil specific microbiological processes in the rock record, which is consistent with the observed patterns in modern analogues.

Keywords

Mat-related structures, elemental geochemistry, biological signal, Palaeoproterozoic, Gabon.

1. Introduction

The *ca*. 2.1 billion-year-old Francevillian sedimentary rocks record significant changes in the Earth's ocean and atmosphere chemistry as they were deposited in the immediate aftermath of the first substantial rise of atmospheric oxygen (Bekker, 2015a; Holland, 2002) and at the time of Earth's longest and most extreme marine positive carbon isotope excursion (Bekker, 2015b; Canfield et al., 2013; El Albani et al., 2010). These sediments record the presence of cm-sized macroscopic fossils with a wide range of characteristics, including lobate, elongated, rod-shaped, and disc-shaped morphotypes (El Albani et al., 2014, 2010), as well as diverse string-shaped structures that have been interpreted as evidence for ancient organism motility (El Albani et al., 2019). In addition, benthic microbial mat communities prevailed in the Francevillian sedimentary deposits (Aubineau et al., 2018; Reynaud et al., 2017) and are now preserved as mat-related structures (MRS) with an exceptional diversity of mat growth patterns (*e.g.*, "elephant-skin" texture, "fairy rings") and mat-protected features (*e.g.*, wrinkle structures) (Aubineau et al., 2018). Based on the observed tufted microtextures and comparison with modern analogues it has been suggested that shallow-marine conditions within the photic zone allowed the development of phototrophic microbial mats composed of oxygenic photosynthesizers such as cyanobacteria (Aubineau et al., 2018; Reynaud et al., 2017). Lastly, these MRS have been shown to record an ancient metabolic activity through a potassium (K)-controlled mineral transformation that occurred during diagenesis (Aubineau et al., 2019).

The observation of MRS in the Francevillian Group offers us the opportunity to further ascertain whether specific chemical "biosignatures" unique to MRS might also be present. This is crucial because organic microbial remnants, preserved as graphite, are common features in early Archean rocks (Dodd et al., 2017; Mojzsis et al., 1996; Nutman et al., 2016; Rosing, 1999; Schidlowski et al., 1979), but these have been subjected to deep burial diagenesis and metamorphism, and as a consequence, without clear physical features of MRS, it is difficult to assess their biogenicity. Indeed, it has been suggested that carbonaceous matter may have been generated abiotically under hydrothermal conditions *via* a process similar to the Fischer–Tropsch synthesis (Brasier et al., 2002; Lindsay et al., 2005; Van Zuilen et al., 2002). Therefore, seeking chemical biosignatures for ancient microbial mats is a sensible way forward because it is well documented that modern microbial mats, comprised of various bacterial species and their extracellular polymeric substances (EPS), are frequently enriched in metal cations at the nmol/g (Huerta-Diaz et al., 2012, 2011; Petrash et al., 2015) to μg/g (Sancho-Tomás et al., 2018; Webster-Brown and Webster, 2007) range. This is a function of the EPS containing a variety of organic functional groups (*e.g.*, carboxyl, phosphate, and sulfhydryl) that deprotonate at circum-neutral pH conditions, thus making them anionic and prone to metal adsorption and potential authigenic mineral nucleation (Konhauser, 1998, 1997). The same functional groups are also responsible for the trapping and binding of detrital particles onto the

88 surface of mats as they grow upward, including heavy mineral grains, such as titanium oxides
89 and zircons (Homann et al., 2015), or clays (Konhauser et al., 1998; Newman et al., 2017,
90 2016; Playter et al., 2017).

91   There is no reason to believe that Precambrian mats behaved differently from the
92 modern so it stands to reason that fossilized mat fabrics should similarly show trace element
93 (TE) enrichments relative to host sediments. In this regard, we measured the bulk TE
94 concentrations of the MRS and host sediments of sandstone and black shale from the *ca.* 2.1
95 Ga Francevillian FB_2 Member of the Francevillian Group in Gabon to ascertain whether
96 potential biological TE enrichments are recorded. These sedimentary rocks were chosen
97 because previous work has already demonstrated that they contain diverse microbial mat
98 morphotypes (Aubineau et al., 2019, 2018), previously described as pyritized MRS, poorly
99 pyritized MRS, and unpyritized "elephant-skin" textures (EST). The rocks also possess
100 geochemical record that tracks Earth's oxygenation history and MRS with associated K
101 enrichment (Aubineau et al., 2019; Canfield et al., 2013; Chi Fru et al., 2019).

102   **2. Geological context of the Francevillian Group**
103 The unmetamorphosed and minimally deformed *ca.* 2.1 Ga old Francevillian Group in
104 southeastern Gabon is a 1.0 to 2.5 km-thick succession that overlies an Archean crystalline
105 basement (Fig. 1a) (Gauthier-Lafaye and Weber, 1989; Weber et al., 2016).
106 Lithostratigraphically, the Francevillian Group has been divided into five formations, labelled
107 FA to FE from the oldest to youngest (Fig. 1b) (Weber, 1968). The Archean crystalline
108 basement is mainly composed of granitoids and greenstone belts (Thiéblemont et al., 2009)
109 with ages *ca.* 3.0–2.9 Ga (Mouélé et al., 2014). The basal FA Formation unconformably
110 overlies the Archean basement and is predominantly composed of fluvial to fluvio-deltaic,
111 coarse- to fine-grained quartz arenites, and conglomerates with minor interlayered mudstones.
112 Collectively, this sedimentary sequence indicates a progressive transition to marine conditions
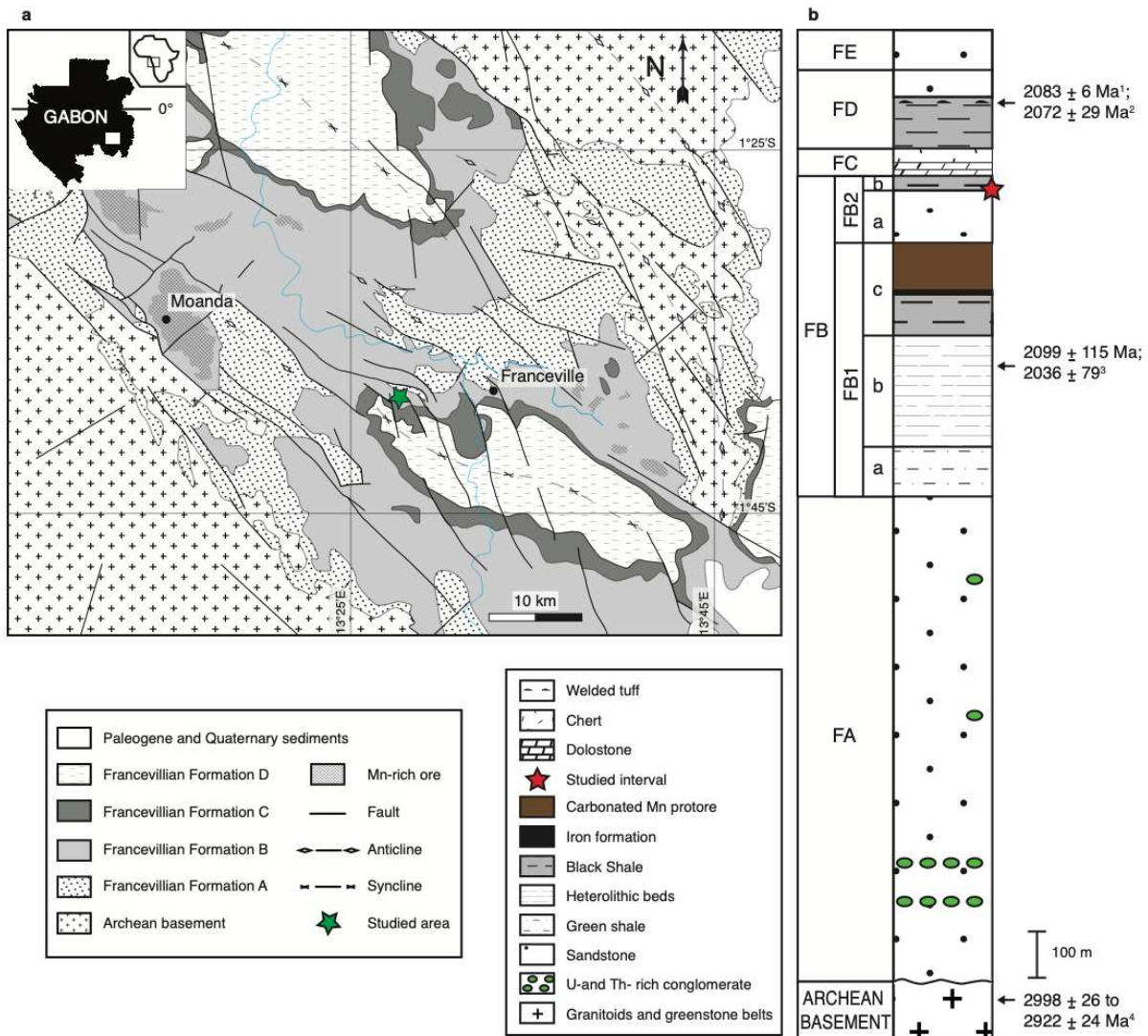113 (Bankole et al., 2015; Gauthier-Lafaye and Weber, 1989).

Figure 1. Geological map of the Paleoproterozoic Franceville sub-basin (**a**) modified from Bouton et al. (2009), showing Gabon in Africa and the Franceville sub-basin in Gabon, and general lithostratigraphic column of the Francevillian Group (**b**). The studied area of the Moulendé Quarry is shown with the green star, while the red star indicates the stratigraphic position of the studied interval with MRS for which synthetic lithostratigraphic column observed in the quarry is shown on Figure 2a. Sources of ages: 1 - Horie et al. (2005); 2 - Thiéblemont et al. (2009); 3 - Bros et al. (1992); 4 - Mouélé et al. (2014).

The predominantly marine FB Formation sedimentary rocks conformably overlie the FA Formation and are characterized by fine-grained sediments with interbedded debris flows, dolostones, thin iron-rich intervals, manganese ore deposits, and sandstones (Gauthier-Lafaye, 1986; Gauthier-Lafaye and Weber, 1989). The FB Formation is classically subdivided into FB_1 (including a, b, and c units) and FB_2 (with a and b units) members based on lithological variations (Azziley Azzibrouck, 1986; Weber, 1968). The FB_1 Member is dominated by greenish, silty to sandy shales, heterolithic beds that consist of shales alternating with interbedded dolomite-cemented siltstones, and manganese-rich black shales (Azziley Azzibrouck, 1986; Pombo, 2004; Reynaud et al., 2017). The FB_2 Member is essentially dominated by coarse-grained sandstones rapidly deposited from high-density gravity currents

5

131 (FB$_{2a}$ unit) that formed largely structureless beds with some intervals showing soft-sediments

132 deformation structures due to dewatering (Reynaud et al., 2017). The sandstones are overlain

133 by black shales with thin interlayered siltstones (FB$_{2b}$ unit), that were deposited during a sea-

134 level fall. Overall, the FB$_2$ Member sediments were deposited in a shallow-marine environment

135 with an oxygenated water column (Canfield et al., 2013; Ossa Ossa et al., 2018). The overlying

136 FC Formation consists of massive dolostone beds, and stromatolitic cherts interbedded with

137 black shales (Amard and Bertrand-Sarfati, 1997; Bertrand-Sarfati and Potin, 1994; Préat et al.,

138 2011; Weber, 1968). An exceptionally well preserved, Gunflint-type microfossil assemblage

139 was recently documented in cherts of the FC Formation, giving additional support to the diverse

140 ecosystem in the Franceville sub-basin (Lekele Baghekema et al., 2017). The FD Formation

141 is mainly dominated by black shales alternating with volcanic tuffs and fine- to medium-grained

142 sandstones (Thiéblemont et al., 2014). The topmost FE Formation consists of medium-grained

143 arkose with interlayered shales (Gauthier-Lafaye and Weber, 1989; Thiéblemont et al., 2014).

144 A number of geochronologic dates has been obtained for the Francevillian Group

145 sediments, but the timing of deposition of the Lower Francevillian Group (FA and FB

146 formations) is still controversial. Diagenetic illites in the FB$_{1b}$ unit yielded a Sm-Nd isotope ages

147 of 2099 ± 115 Ma and 2036 ± 79 Ma on <0.4 μm and <0.2 μm clay fractions, respectively,

148 which constrained the age of early diagenesis in this unit (Bros et al., 1992). Finally, the

149 depositional age of the FD Formation is well constrained with ignimbrite tuffs and sandstones

150 that provided U-Pb ages of 2083 ± 6 Ma (Horie et al., 2005) and 2072 ± 29 Ma (Thiéblemont

151 et al., 2009), respectively. Based on carbonate and organic carbon isotope compositions, the

152 FB and FC formations record the end of the Lomagundi carbon isotope excursion (Canfield et

153 al., 2013; El Albani et al., 2010; Préat et al., 2011), dated elsewhere between 2.11 and 2.06

154 Ga (Karhu and Holland, 1996; Martin et al., 2013). Given these age constraints, deposition of

155 the Francevillian Group likely occurred *ca*. 2.1 Ga ago, during a critical juncture when Earth's

156 atmosphere underwent a critical transition towards persistently oxygenated conditions.

157 **3. Methods**

158 **3.1. Sampling**

159 Highly diverse microbial mats and their host sediments were sampled from the Moulendé

160 Quarry, Franceville sub-basin, Gabon. The mat layers were carefully separated from the

161 underlying sediments with a blade, avoiding contamination with the underlying sediments.

162 Directly from below the MRS, the host sediments were also sampled for geochemical analyses.

163 **3.2. Microscopy**

164   Mineral composition and textural relationships were studied in polished and carbon-coated thin

165   sections, using a FEI Quanta 200 scanning electron microscope (SEM) equipped with an

166   energy-dispersive X-Ray Spectrometer (EDX) as previously described (Aubineau et al., 2018).

167   ### 3.3.   Major and trace element analyses

168   Whole-rock geochemical analyses of major and trace elements were performed on 7 pyritized

169   MRS, 7 poorly pyritized MRS, 4 unpyritized "elephant-skin" textures, 7 sandstones, and 15

170   black-shale samples. Major element (Si, Al, Fe, Mn, Mg, Ca, Na, K, Ti, and P) concentrations

171   were measured by inductively-coupled plasma optical emission spectrometry (ICP-OES), while

172   trace and rare earth element (As, Ba, Bi, Cd, Ce, Co, Cr, Cs, Cu, Dy, Er, Eu, Gd, Hf, Ho, La,

173   Lu, Mo, Nb, Nd, Ni, Pb, Pr, Rb, Sb, Sm, Sn, Sr, Ta, Tb, Th, Tm, U, V, W, Y, Yb, Zn, Zr) contents

174   were analyzed by inductively coupled plasma mass spectrometry (ICP-MS) at *Service*

175   *d'Analyse des Roches et Minéraux* (SARM) of the *Centre de Recherches Pétrographiques et*

176   *Géochimiques* (CRPG), Nancy, France. Total sulfur content of the MRS and host sediments

177   was measured by infrared absorption with a carbon-sulfur EMIA 320-V2 (HORIBA) at SARM-

178   CRPG.

179   Prior to analysis, each sample was powdered in an agate mortar. The glass beads were

180   then prepared by fusion with ultra-pure lithium metaborate ($LiBO_2$) at 980 °C followed by a

181   dissolution in a 1 mol/L nitric acid, 0.5% hydrogen peroxide, and 10% glycerol mixture. The

182   analytical accuracy and precision were found to be better than 5% for major elements, with the

183   exception of Ca (10%) and P (>25%). According to the analyzed trace element concentrations,

184   the uncertainty is lower than 5–10% for elemental concentrations > 50 ppm, less than 5–20%

185   for elemental concentrations between 10 and 1 ppm, and higher than 25% for elemental

186   concentrations near the detection limit (Carignan et al., 2001).

187   The enrichment factor (EF; cf. Tribovillard et al., 2006) relative to the average shale

188   was used to assess whether an element was authigenically enriched or depleted. The EF is

189   considered to be detectable and substantial when it is >3 and >10, respectively (Algeo and

190   Tribovillard, 2009). EFs were calculated as $(X/Al)_{sample}/(X/Al)_{average\ shale}$, where X stands for the

191   element concentration. Descriptive statistics for trace elements was performed with R software

192   (version 3.5.1; R Core Team, 2018) to enhance data resolution relative to the number of

193   individual samples within each lithology.

194   ### 3.4.   X-ray fluorescence (XRF) microscopy

195   Scanning X-ray fluorescence microscopy analysis was performed on polished slab sections of

196   representative MRS samples. The XRF elemental distribution maps were collected on several

197   areas within the investigated samples at the Nanoscopium hard X-ray nanoprobe beamline

198   (Somogyi et al., 2015) of Synchrotron Soleil (L'Orme des Merisiers Saint-Aubin, France). The

199   monochromatic X-ray beam with 12 keV energy was focused on the sample by a Kirckpatrick-

200   Baez nano-focusing mirror. We used the fast continuous scanning (FLYSCAN) technique to

201   obtain micrometer resolution for elemental maps of mm_2—sized sample areas (Medjoubi et

202   al., 2013). We have increased the solid angle of detection by the means of two Si-drift detectors

203   (VITUS H50, KETEK GmbH) to collect full XRF spectra in each pixel of the scans. We provide

204   the distribution of Fe, As, and Ni with micron-scale spatial resolution and high analytical

205   sensitivity. Each elemental map was normalized to 10 ms/pixel exposure time.

206   **4.   Results**

207   **4.1.   Textural diversity of MRS**

208   Mat-related structures, marine shales, and sandstones collected from across the FB_2 Member

209   (Fig. 2a) are different in their macroscopic and microscopic textures, mineralogy, and

210   geochemistry (Figs. 2b-g; Tables S1, S2). Pyritized MRS are developed on top of thin bedded,

211   parallel-laminated black shales. They range from 0.8 to 3 mm in thickness and contain

212   euhedral pyrite crystals, 20 to 30 μm in size (Figs. 2b, c). In this study, pyritized MRS refer to

213   flat, pyritized structures, domal buildups, and "fairy ring" features that were previously

214   described by Aubineau *et al*. (2018) in the same rocks. The poorly pyritized MRS from the

215   sandstone unit reflect mat growth or mat-protected (resulting from mat preservation of

216   structures formed independently from mat growth) patterns (cf. Aubineau et al., 2018; Sarkar

217   et al., 2008). They vary between 0.2 and 0.5 mm in thickness (Figs. 2d, e), and contain a large

218   number of detrital minerals (Fig. 2e; Fig. S1) (Aubineau et al., 2018). Among them, randomly

219   arranged zircons and titanium oxides, and clay particles up to 100 μm in size, are common.

220   Numerous sub-euhedral to euhedral pyrite crystals with varying size, but generally smaller than

221   those in the pyritized MRS, were observed at deeper levels in the poorly pyritized MRS (Fig.

222   S2). In addition, interpreted gas escape and bubble-like structures, having clay minerals

223   disorganized at the edges, but aligned around them, were likely formed before compaction

224   (Fig. 2e). The unpyritized EST, some of which developed on the same bedding planes in

225   sandstones as the poorly pyritized MRS, is one of the most common mat morphologies,

226   characterized by tufted microbial fabrics (Figs. 2f, g) (Aubineau et al., 2018; Reyes et al., 2013;

227   Shepard and Sumner, 2010). They reach up to 2 mm in thickness and lack embedded heavy

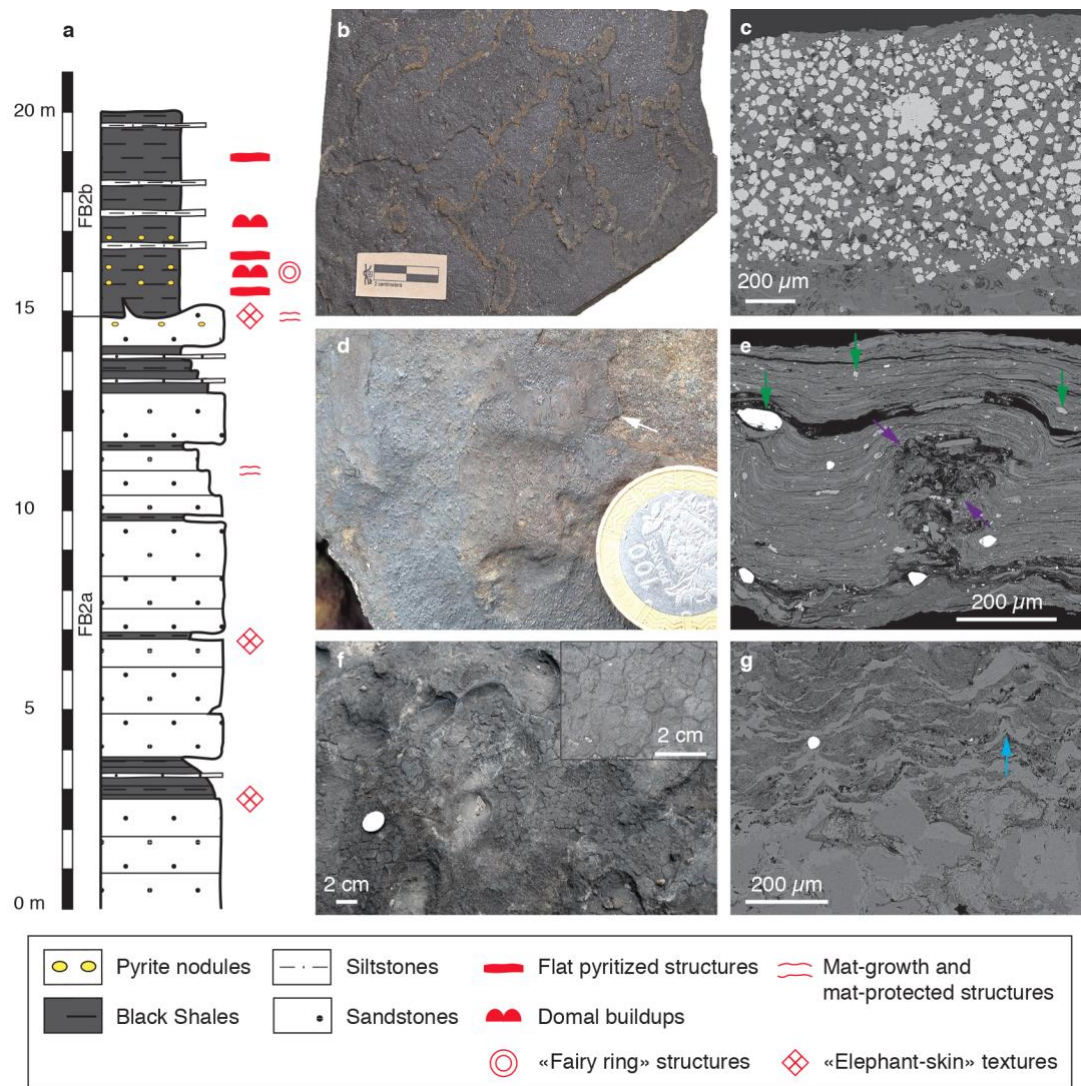228   minerals and putative gas escape structures.

Figure 2. Lithostratigraphic column and representative mat-related structures (MRS) with their associated petrographic textures from both sandstone and black shale facies. **a,** Composite lithostratigraphic section of the FB$_2$ Member in the studied area showing stratigraphic levels where pyritized MRS (flat pyritized, domal buildup, and 'fairy ring' structures), poorly pyritized MRS (mat-growth and mat-protected structures), and unpyritized MRS (EST: "elephant-skin" texture) developed. **b,** Flat pyritized MRS from the FB$_{2b}$ unit. **c,** SEM image of pyritized MRS in cross-section perpendicular to the bedding plane. Note that pyrite grains and clay particles are developed within biofilms. **d,** Mat-layer structures (white arrow) on the bedding surface of sandstone from the FB$_{2a}$ unit. **e,** SEM image of micrometer-thick poorly pyritized MRS in cross-section perpendicular to the bedding plane. Green and purple arrows show trapped and bound heavy minerals and a gas escape structure, respectively. **f,** EST from the FB$_{2a}$ unit. Inset box shows reticulate pattern. **g,** SEM image of tufted microbial fabrics from the EST above the poorly sorted quartz sandstone. Blue arrow points to tufted microbial fabrics. Images in b and c, and f and g are modified from Aubineau *et al.* (2018) and Aubineau *et al.* (2019), respectively.

4.2. Provenance characterization

The host sediments have similar chondrite-normalized rare earth elements (REE) + Y patterns (Fig. 3a; Table S2). The steep light-REE pattern with a flat heavy-REE profile in the post-

246   Archean shales reflects REE abundances in the upper continental crust exposed to weathering

247   (Large et al., 2018; Taylor and McLennan, 2001). REE contents decrease with increasing SiO_2

248   content, reflecting quartz dilution. The similar REE + Y patterns of sandstone and black shale

249   lithologies suggest that the sediments on which the MRS developed had the same provenance.

250   Furthermore, sandstones and black shales are interlayered (Fig. 2a), indicating that they were

251   deposited in the same general setting, but at different energy levels (cf. Reynaud et al., 2017).
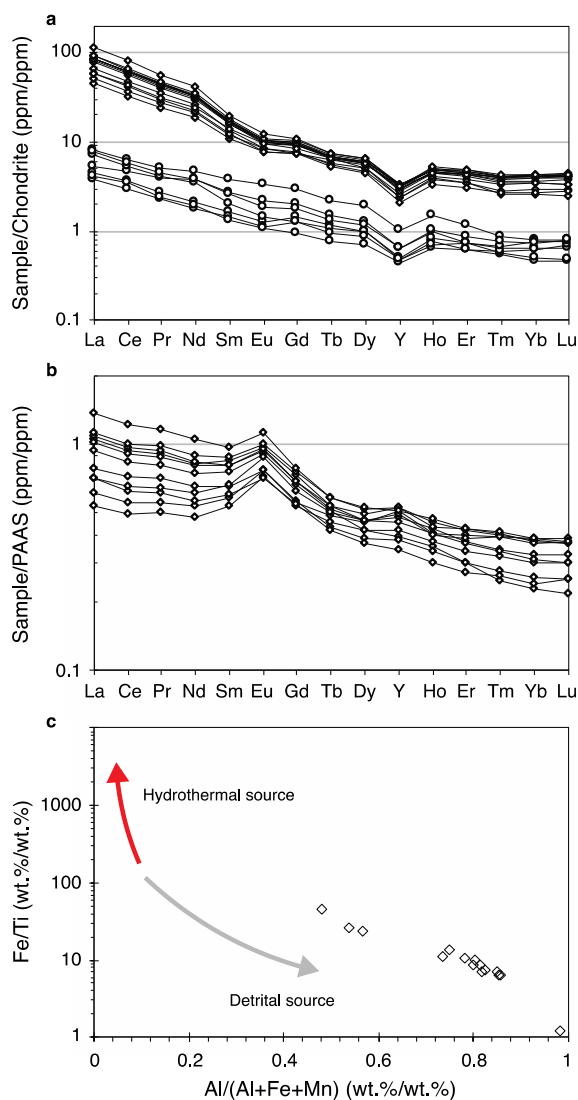

252

Figure 3. Geochemistry of the host rocks, black shales (diamonds) and sandstones (circles). **a,**
Chondrite-normalized REE + Y patterns. Chondrite values are from Schmitt et al. (1964) and Evensen
et al. (1978). **b,** PAAS-normalized REE + Y patterns. PAAS values are from Taylor and McLennan
(1985). **c,** Binary plot of Fe/Ti *vs.* Al/(Al+Fe+Mn) after Pecoits et al. (2009).

257   The REE abundances have been normalized to the Post-Archean Australian Shale

258   (PAAS), hereafter referred to as REE(SN) (Fig. 3b). The latter is a widely used reference for

259   normalizing sedimentary lithologies, allowing easy comparison with previous studies. The

260   PAAS-normalized REE + Y patterns of black shales from the FB$_2$ Member show moderately

261   positive Eu anomalies (Eu/Eu*; see Table S2 for method of calculation), ranging from 1.29 to

262   1.44. A strong positive Eu anomaly in sediments is usually interpreted to indicate high-

263   temperature hydrothermal fluxes to the water column (Bolhar et al., 2004; Hiebert et al., 2018;

264   Planavsky et al., 2010). Moreover, the REE + Y patterns reveal a moderately steep trend with

265   light-REE enrichments, as shown by $Pr/Yb_{(SN)}$ ratios ranging between 1.45 and 3.54 (Fig. 3b;

266   Table S2). In addition, the binary plot of Fe/Ti *vs*. Al/(Al+Fe+Mn), which resolves the influence

267   of a hydrothermal *vs*. detrital source (Fig. 3c; cf. Pecoits *et al.* 2009), suggests that the studied

268   black shales predominantly reflect a detrital source, with limited hydrothermal influence.

269   Similarly, the average Y/Ho value of 31.4 (Table S2) is lower than the modern seawater Y/Ho

270   ratio that is >44, but above the invariable Y/Ho ratio of continental crust (~26; Bolhar et al.,

271   2004).

272   ### 4.3.   Chemical composition of host sediments and MRS

273   Petrographic analysis showed that Fe-(oxyhydr)oxide coatings were not found around the

274   pyrite crystals (Figs. 2c, S2). In addition, the X-ray diffraction patterns of the Francevillian MRS

275   and host sediments revealed the occurrence of pyrite as the main iron sulfide, while Fe-

276   (oxyhydr)oxides were lacking (Aubineau et al., 2019). Combined petrographic and XRD

277   analyses suggest that chemical composition of our samples was not appreciably affected by

278   recent oxidative weathering.

279   Descriptive statistical relationships among independent TE variables of MRS and

280   individual sediment lithologies show the largest variation along the first and second Principal

281   Components (PC) (Fig. 4a). Collectively, both PC explain more than 78% of the total variance

282   in the dataset (Table S3). According to the contribution of each variable along the PC1, the

283   variation is induced by TE that are usually taken to be proxies of the detrital flux (Fig. 4b;

284   McLennan 1989, 2001; Tribovillard *et al.* 2006). Along the PC2, it appears that the metals

285   enriched in pyrite, apart from Cd and Zn, are responsible for differences amongst the

286   lithologies. The PC1 accounts for 54.3% of the total variance, with the poorly pyritized MRS

287   being different from the pyritized MRS, EST, and host sediments (Fig. 4a). Interestingly, EST,

288   pyritized MRS, and black shales do not cluster into distinctly separate groups. Their spread

289   along the PC1 axis seems largely determined by the elements that are abundant in the heavy

290   mineral fraction, as indicated by the large contribution of Zr and REE (Fig. 4b). This is

291   consistent with petrographic observations that indicate the presence of detrital zircon and Ti-

292   oxides in the poorly pyritized MRS. The PC2 contributes 24.4% to the total variance, with the

293   pyritized MRS plotting above the poorly pyritized MRS, EST, and host sediments. The pyrite

294   content likely controls their spread along the PC2 axis. One pyritized MRS sample has a

295   signature similar to that of black shales, suggesting either a large contribution of the host

sediment during sample separation or a depletion in metals enriched in pyrite compared to the other pyritized MRS (Fig. 4a).
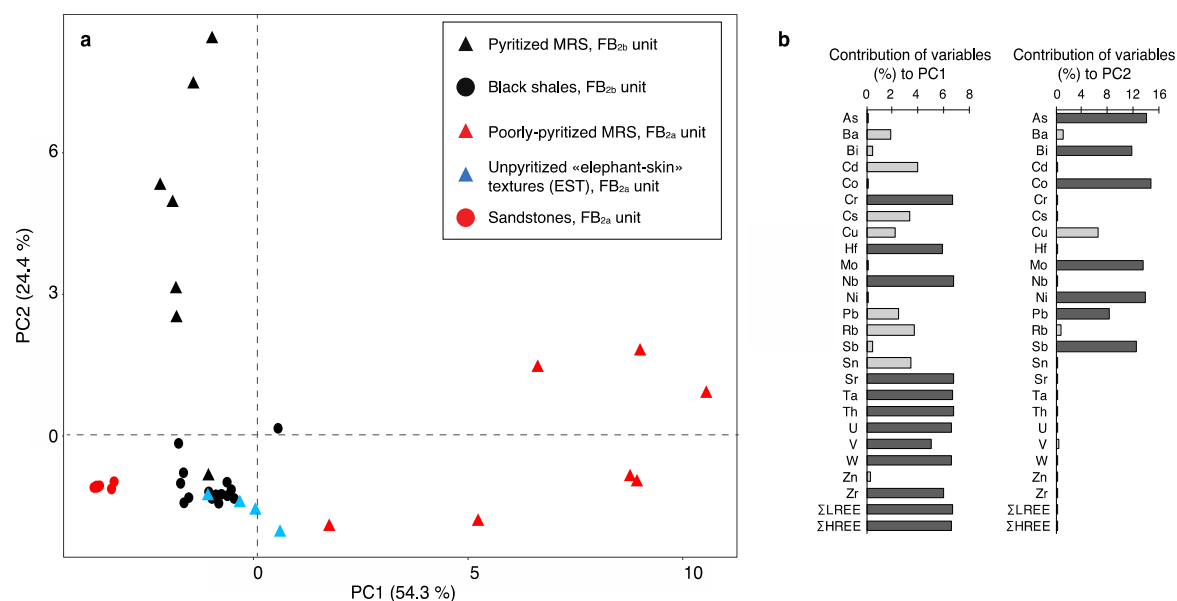

Figure 4. Descriptive statistical treatment. **a,** Principal component analysis of 40 individuals representing the relationships among 3 MRS morphotypes and 2 host sediments (black shales and sandstones) and 26 independent variables (trace element concentrations). **b,** Contribution of each variable (%) along PC1 (left) and PC2 (right). The stronger the contribution of TE, the darker the bar is.

Stratigraphic geochemical profiles of the FB_2 Member reveal dramatic difference in bulk composition among the three MRS morphotypes even on the same stratigraphic level, but also heterogeneous composition of the poorly pyritized and pyritized MRS (Fig. 5). In the poorly pyritized MRS samples, EFs have a mean of 2.1 for Ti (EF_{Ti}) and 6.6 for Zr (EF_{Zr}), suggesting moderate to strong enrichment, respectively. These elements are predominantly depleted to moderately enriched in the EST (mean EF_{Ti} = 0.2; mean EF_{Zr} = 2.5) and in the pyritized MRS (mean EF_{Ti} = 0.3; mean EF_{Zr} = 0.5). Chalcophile elements (CE) are depleted to weakly enriched (mean EF_{As} = 0.1; mean EF_{Ni} = 1.1) and weakly enriched (mean EF_{As} = 1.4; mean EF_{Ni} = 2.0) in the EST and the poorly pyritized MRS, respectively. On the other hand, the pyritized MRS are strongly enriched in CE (mean EF_{As} = 13.2; mean EF_{Ni} = 14.5). The host sediments (both sandstone and black shale) show no enrichment to weak TE enrichment for most samples, with mean EFs for Ti, Zr, As, and Ni of 0.4, 1.5, 0.5, and 1.2, respectively (Fig. S3).
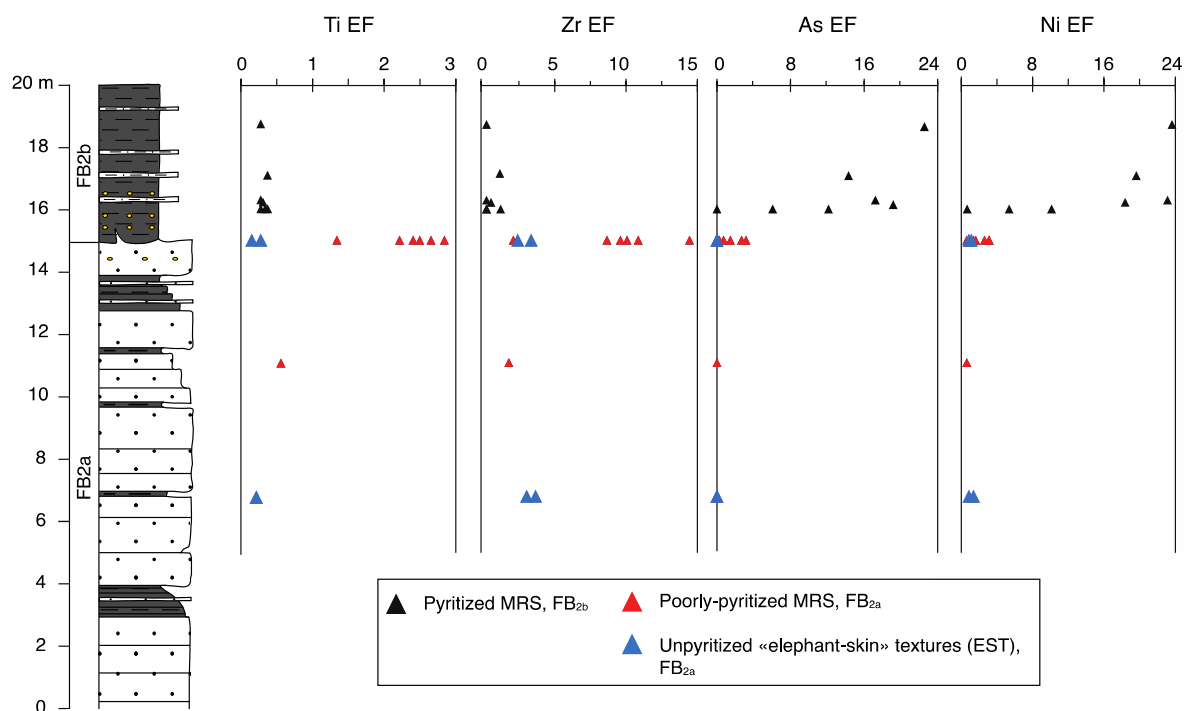
Figure 5. Stratigraphic profile of enrichment factors (EF) of selected detrital and chalcophile elements within MRS. EF are normalized to the average shale (Ti, Zr, and Ni concentrations for the average shale are from Taylor and McLennan (2001) and As concentration for the average shale is from Li and Schoonmaker, 2003).

Generally, CE are enriched within the sediment in association with S-bearing minerals, and when plotted against each other, show positive covariation. The trends found within the MRS and black shales from the FB₂ Member show more or less the expected pattern for the preferential incorporation of CE into sulfide minerals (Figs. 6a, b). The mixing trends associated with the poorly pyritized MRS, EST, and host shale reflect the variable content of CE-bearing pyrite. Nonetheless, the correlation trends of pyritized MRS differ from those of pyrite-poor MRS and host sediments, indicating that either some intrinsic properties (*e.g.*, mineralogy, organic matter, or microbial sulfate reduction rate) or the dynamic fluctuations in supply of CE controlled incorporation of pyrite-hosted metals. For instance, organic substrate may have controlled the availability of CE as the carbonaceous material of MRS and host rocks was derived from different sources (*i.e.*, benthic *vs.* planktonic origin). Minor to no contribution of benthically produced organic matter to the host sediments, which is suggested by the lack of microbial mat structures (Aubineau et al., 2018) and K enrichment (Aubineau et al., 2019), argues for two distinct carbon sources. Specifically, K incorporation occurred during the living stage of benthic MRS through a bacterially mediated process, whereas the sinking flux of particulate organic material did not incorporate and deliver K to the sediments to the same extent. Moreover, 43% ($R^2=0.43$) of total co-variation in the pyritized MRS between CE and S (Fig. 6a) implies that CE are also associated with other components. However, this relationship might be biased as it seems to be controlled by the one pyritized MRS sample with lower CE

13

content, by a factor of 10 to 100, and moderate S concentration. It reveals high heterogeneity in CE contents in pyritized MRS.
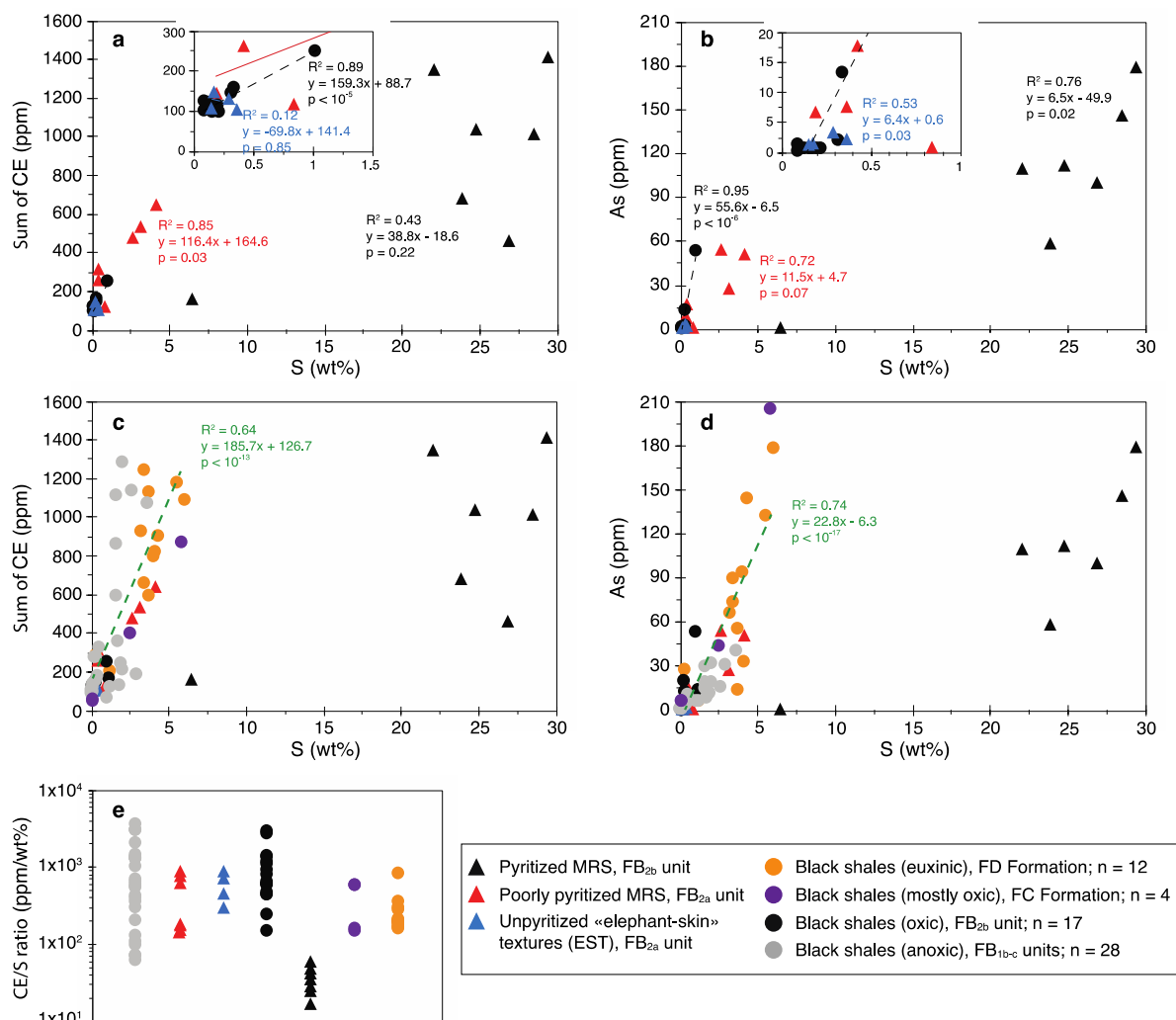

Figure 6. Relationship between chalcophile elements and bulk-rock sulfur in pyritized MRS, poorly pyritized MRS, unpyritized "elephant-skin" textures (EST), and Francevillian Group black shales (from the FB$_{1b}$ and FB$_{1c}$ units and the FD Formation). **a,** Cross plot of Σchalcophile element (As, Bi, Co, Cu, Mo, Ni, Pb, and Sb) contents vs. bulk-rock S concentrations for MRS and host black shales. **b,** Cross plot of As content vs. bulk-rock S concentration for MRS and host black shales. Insets (a and b) show co-variation at low CE and S contents. **c**, Cross plot of Σchalcophile (As, Bi, Co, Cu, Mo, Ni, Pb, and Sb) contents vs. bulk-rock S concentrations for MRS and all the Francevillian Group black shales (green trend). **d,** Cross plot of As contents vs. bulk-rock S concentrations for MRS and all the Francevillian Group black shales (green trend). **e,** CE/S ratios for 3 MRS morphotypes and 2 host sediments (black shales and sandstones). CE and S contents for black shales of the Francevillian Group are from Canfield *et al.* (2013). p-value (p) is provided with a confidence level of 95%. Data for some samples are below the detection limit; in that case a value of half of the detection limit was used.

Compiled data for CE and S contents of the Francevillian Group black shales (from the FB$_{1b}$ unit to FD Formation) illustrate an overall linear relationship (Fig. 6c), suggesting that sulfide production controlled the enrichment in CE. The strong positive co-variation (R²= 0.64) for black shales of the Francevillian Group suggests that CE contents are only moderately controlled by other mineral phases. The pyritized MRS show a different trend with higher S

14

contents for the same CE concentrations. The same trend is also observed for As and S (Fig. 6d), indicating that the As content was affected by the same processes that controlled CE enrichments. Finally, the CE/S ratios of pyrite-poor MRS and the Francevillian Group black shales are mostly within the same range from 10_2 to 10_3, whereas the pyritized MRS show the lowest ratios down to 17 (Fig. 6e).

4.4. High-resolution metal distribution in the MRS

Millimeter-sized areas of each MRS morphotype were analyzed by synchrotron-based scanning X-ray fluorescence microscopy revealing spatial variations in S, K, Ca, Ti, Ce, Ba, Cr, Mn, Fe, Ni, Cu, Zn, Ga, Ge, Hf, and As. The distribution maps of Fe, As, and Ni are shown in Figures 7 and 8. Pyrite crystals are highlighted by Fe distribution and location of CE by Ni and As maps. Although some Fe is hosted in phyllosilicates, the highest abundance of iron is in pyrite grains, highlighting the difference amongst the MRS. EST have Ni and As concentrations close to the detection limit (Fig. 7a). These elements are unlikely to be associated with pyrite, since pyrite is not present at a detectable level in the same spots. This also applies to the absence of a strong relationship between CE and S in the EST. The poorly pyritized MRS contain higher CE concentrations relative to the EST that are heterogeneously distributed in pyrite grains (Fig. 7b). A few small, euhedral pyrite crystals display As-rich cores. Arsenic is preferentially located within the pyrite cores in the pyritized MRS with a variation in As content of $\pm 10\%$ (1 SD), whereas Ni is mostly concentrated within the overgrowths (Fig. 7c). This pattern suggests high As content in early pore-waters from which pyrite cores nucleated and higher Ni content during later diagenesis when the overgrowths were formed. Arsenic distribution within individual pyrite crystals is heterogeneous, resulting from micrometer-thick As-rich rims around the cores and a decrease in As content toward the crystal surface (Fig. 8). Ni also exhibits a highly variable abundance pattern often with a micrometer-thick Ni-rich zone at the pyrite crystal surface. CE appear to be enriched by a factor of 15 (As) and 6 (Ni) in pyritized MRS compared to poorly pyritized MRS.
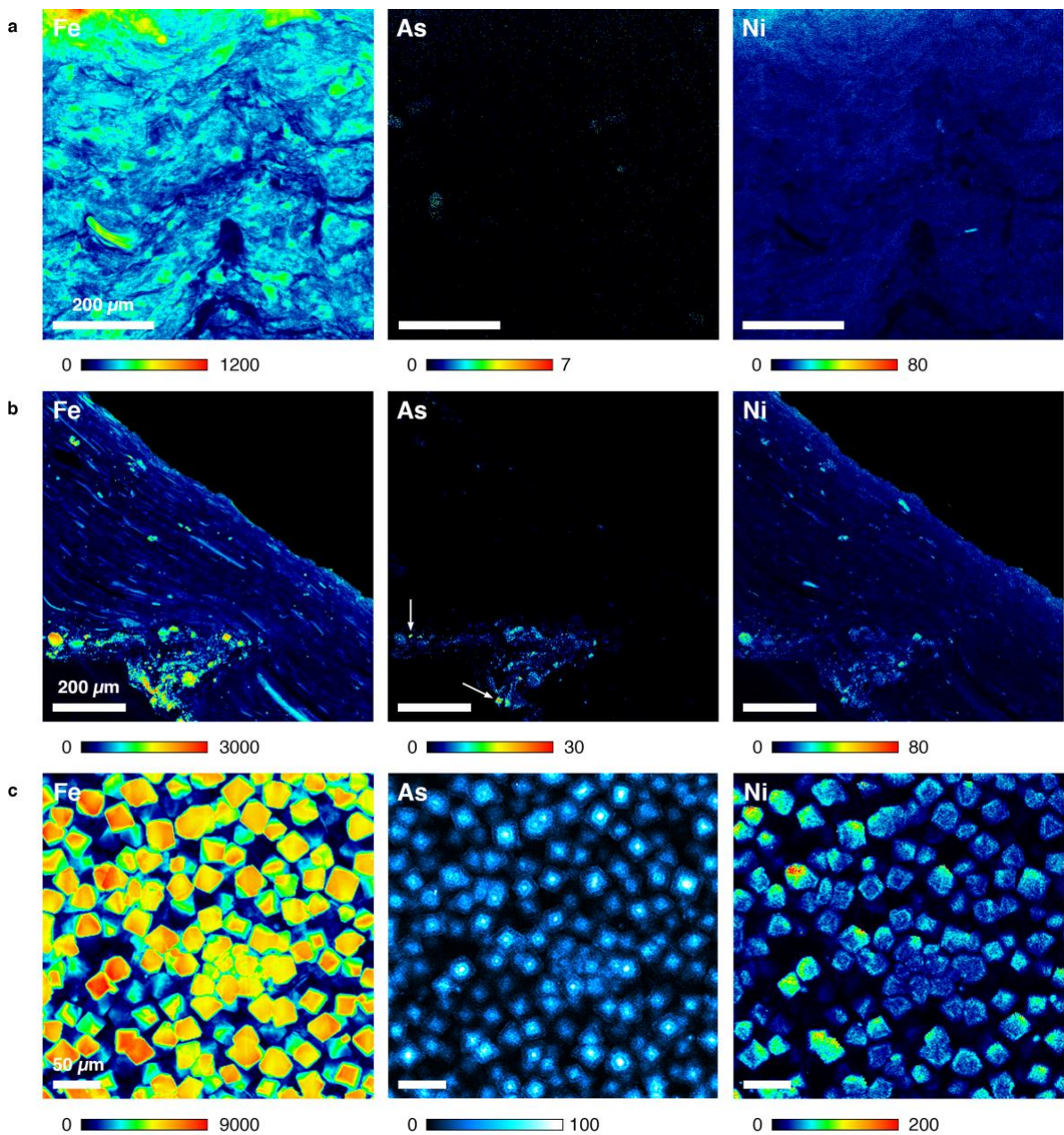
Figure 7. Synchrotron-based XRF microscopy showing distribution of Fe, As, and Ni. **a**, unpyritized EST. **b**, poorly pyritized MRS. White arrow indicates As-rich pyrite core. **c**, pyritized MRS. Colour bars indicate intensity scale of the metal XRF distribution maps in counts/10 ms (black colour indicates concentrations below the detection limit). Higher XRF intensities correspond to higher metal contents.
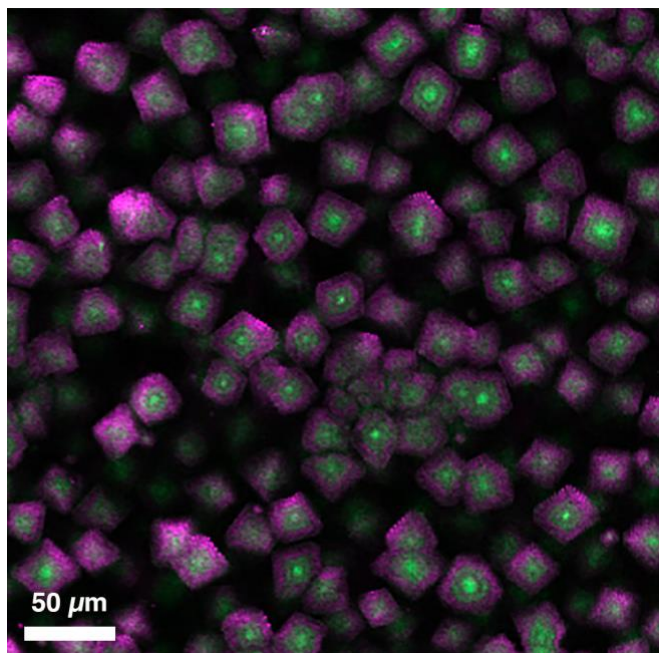
Figure 8. Composite image: As (green) and Ni (magenta) XRF maps for pyritized MRS.

5. Discussion

5.1. Microbial fabric and response to the environment

At high concentrations of suspended material in the water column, laboratory-cultured cyanobacteria can become rapidly coated with clay minerals, which means that they may preserve the TE and mineralogical context of detrital input to the depositional setting in which they lived (Newman et al., 2017, 2016; Playter et al., 2017). The Francevillian poorly pyritized MRS and EST contain in a high abundance TE-bearing heavy minerals relative to the host sandstone facies. The absence of heavy mineral enrichment in the overlying pyritized MRS reflects a significant decrease in sedimentation rate and energy in the depositional setting (Fig. 9a), consistent with a change in sediment supply from sand-rich high density flows to fine-grained black shales (Reynaud et al., 2017). As such, the distribution of heavy minerals in the Francevillian Group MRS, or for that matter any MRS, is best explained by passive trapping and binding processes (Sforna et al., 2017).

Importantly, poorly pyritized MRS and EST developed along the same uppermost stratigraphic horizon in coarse-grained sediments (Fig. 9a). Although the transition from sandstone to black shale might imply a transgressive surface, the sandstones of the FB Formation were deposited from pulses of high density flows into a depositional setting with a background mud sedimentation (Reynaud et al., 2017). It is thus reasonable to assume that the poorly pyritized MRS and EST were formed under exactly the same depositional conditions. The variable abundance of Ti- and Zr-bearing heavy minerals in these mats only few meters apart likely reflects minor changes in environmental conditions under which the

17

MRS flourished (*e.g.*, hydrodynamic regime or sediment delivery pattern) (Fig. 9a). These changes appear to have impacted microbial growth patterns, resulting in a shift to different mat morphology (Fig. 9a). Indeed, numerous observations on stromatolite morphology have shown active adaptation by the bacterial community to environmental conditions, such as water energy and the availability of light and nutrients (*e.g.*, Allwood et al., 2006; Jahnert and Collins, 2012; Petrash et al., 2012). Similarly, distribution patterns of distinct microbial mat morphotypes across ancient tidal flats constrain palaeoenvironmental conditions (Bose and Chafetz, 2009; Homann et al., 2015; Sarkar et al., 2014).

The poorly pyritized MRS typically display the smallest mat thickness and planar morphologies that likely reflect a morphological adjustment to high energy hydrodynamic regime, while the EST and pyritized MRS show larger mat thicknesses and well-developed mat-growth fabrics (*i.e.*, tufted features, domal buildups) that likely indicate optimal growth conditions (e.g., Gerdes et al., 2000). Differences in physical environmental conditions would have also led to highly variable abundance of TE-bearing heavy minerals in the Francevillian Group MRS and may have triggered ecologically controlled growth (Fig. 9a). While mat morphology and thickness are linked to external environmental factors, it has been recently documented that the mat thickness may similarly influence the community structure (Suarez et al., 2019). This leads to different redox profiles and internal carbon recycling styles amongst the microbial communities since thick mats contain a well-expressed anoxic area in the mat structure, whereas thin mats create only a limited anoxic region (Suarez et al., 2019). However, effects of thickness on microbial architecture are difficult to quantify because the hydrodynamic regime (Battin et al., 2003; Flemming et al., 2016), water depth (Lydmark et al., 2006), temperature (He et al., 2016), and dissolved carbon to nitrogen ratios (Okabe et al., 1996) also impact on the microbial community structure. Thus, in combination, these environmental parameters might have promoted the lack or poor expression of an anoxic zone in the thick unpyritized EST (Fig. 9b).
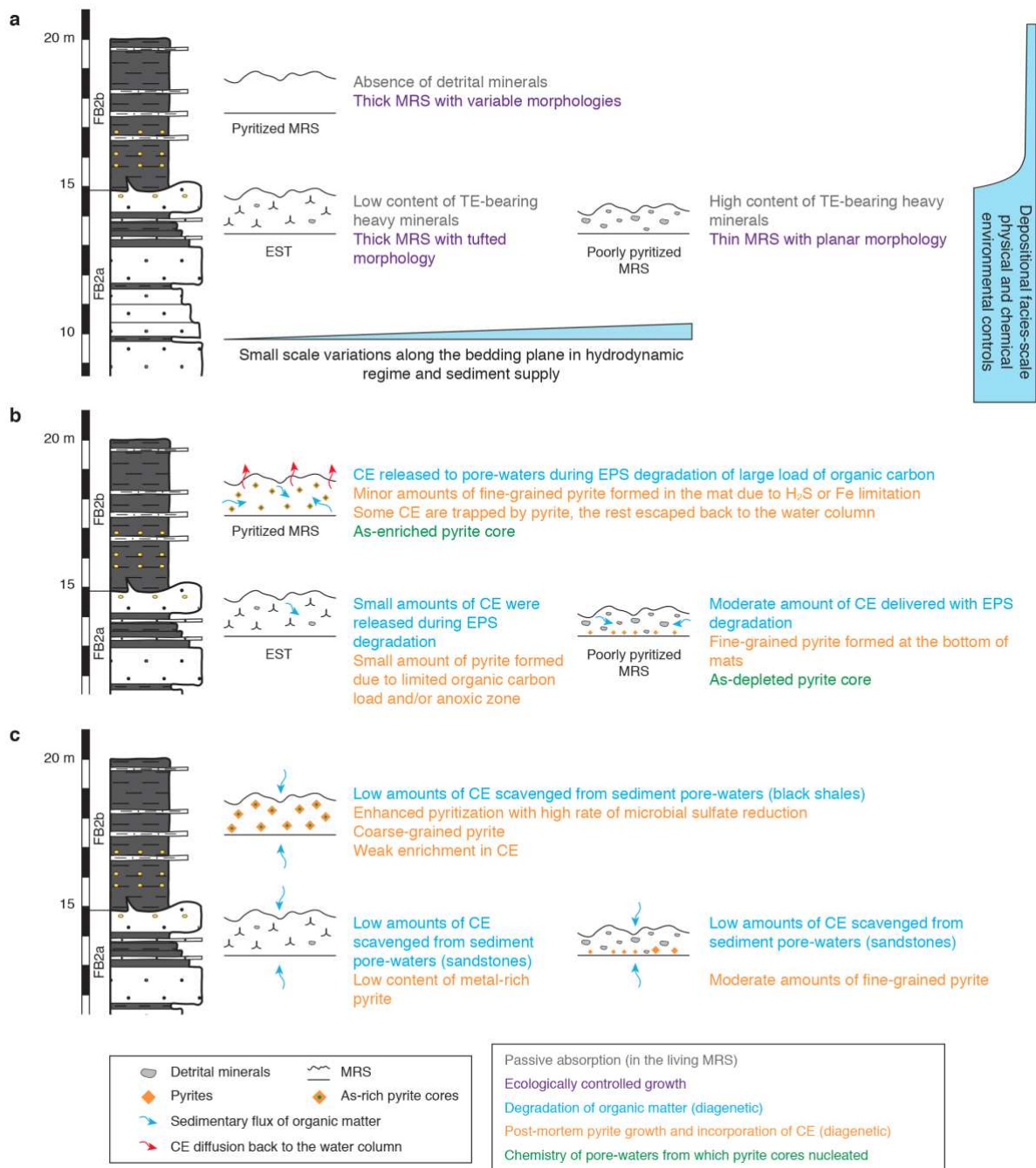
Figure 9. Conceptual model for the spatial and temporal TE variations in the Francevillian Group FB₂ unit MRS. **a,** processes that took place during the living stage of mats. Depositional, small-scale to facies-scale environmental factors controlled the distribution of heavy minerals in the Francevillian MRS. The external mat morphologies provide information on local ecologic conditions. **b**, short-lived, first stage of pyrite formation on the earliest phase of diagenesis. The EPS degradation resulted in the release of CE to pore-waters. The amount of CE delivered with EPS decay should be proportional to the organic carbon content that is buried. Depending of sulfur and Fe availability, CE were trapped by fine-grained pyrite or diffused back to the water column. **c**, long-lived, second stage of pyrite formation as diagenesis progressed. The remaining organic matter was degraded and, thus, larger amounts of H₂S and Fe were released to pore-waters. High concentrations of biogenic H₂S were locally produced, but only small amounts of CE were scavenged into coarse-grained pyrite.

5.2. Microbial mineralization

19

453 Recent studies on transition metals and metalloids associated with present-day hypersaline
454 mats (Huerta-Diaz et al., 2012; Petrash et al., 2015; Sancho-Tomás et al., 2018; Sforna et al.,
455 2017) have revealed that TE can be trapped by and bound to the organic matrix, progressively
456 accumulating with depth via incorporation into sulfides. The latter form as the original mat
457 organic material is degraded by the activity of anaerobic heterotrophs (*e.g.*, sulfate-reducing
458 microorganisms), eventually diminishing the cation-binding capacity of the EPS matrix (Dupraz
459 et al., 2009; Dupraz and Visscher, 2005). Then, as authigenic pyrite forms by the reaction of
460 reactive Fe and biogenic H_2S, metals liberated from mats to pore-waters are scavenged into
461 sulfidic microenvironments where pyrite crystals grow (Fig. 9b), resulting in high spatial
462 variability of metal distribution (Huerta-Diaz et al., 2012; Sforna et al., 2017). The spatial
463 restriction of pyrite grains to deeper levels in the mat in the poorly pyritized MRS or their
464 development over the entire mat structure in the pyritized MRS likely reflects the extent of the
465 sulfidic region (Fig. 9b).

466 The pyrite overgrowths in the MRS that formed later during diagenesis precipitated from
467 pore-waters that were no longer enriched in As, but in Ni (Fig. 9b). Alternatively, the preferential
468 incorporation of As into the early pyrite phase and Ni in the later phase may simply suggest
469 that these two elements have different kinetic behavior whereby As is more reactive towards
470 H_2S than Ni (cf. Huerta-Diaz and Morse, 1992). Hydrothermal fluids affecting sediments during
471 diagenesis could produce CE-rich pyrite rims (Large et al., 2009), but we have no evidence for
472 migration of such fluids or late-stage remobilization that could account for strongly enriched
473 CE in pyrite rims during late diagenesis. Variability in concentration of pyrite-hosted metals in
474 the three microbial mat morphotypes is mainly linked to the sulfide production and
475 concentration in pore-waters (Figs. 9b, c). The relationship between CE and total S is,
476 however, complicated since whole-rock data seem to reflect several host minerals. Some of
477 these CE might be incorporated into clays, scavenged by organic matter, and/or absorbed onto
478 the surface of Fe oxides (Chappaz et al., 2014; Chi Fru et al., 2019; Nachtegaal et al., 2005),
479 which might explain weak to moderate correlations within each MRS morphotype.

480 ### 5.3. Implications of weak enrichment in CE in the pyritized MRS
481 The CE enrichment is not unique to the MRS, but instead typical for the depositional setting of
482 the Francevillian Group where seawater and pore-water sulfide levels controlled their
483 incorporation into sediments. Although a moderately positive Eu anomaly is observed, low
484 Y/Ho and Fe/Ti ratios in combination with high Al/(Al+Fe+Mn) ratios (see Fig. 3) do not support
485 a strong influence of hydrothermal fluids on the depositional site, and rather suggests that CE
486 were supplied by continental weathering. Consistent with this interpretation, large variations in
487 CE/S ratios for the Francevillian Group shales (FB_{1b-c} units, and FC and FD formations) were

not observed. However, absence of substantial CE enrichment in the pyritized MRS is unexpected because they contained appreciable amounts of carbonaceous materials to maintain extensive pyritization. The pyritized MRS samples with high bulk-rock S concentrations have lower CE/S ratios than the Francevillian Group sediments, which requires an explanation for the weak enrichment in CE.

Weak enrichment in CE in the pyritized MRS might reflect a change in aqueous fluxes of CE to the ocean during the living stage of the MRS, but this would not explain the similar range of CE content in the pyrite-poor MRS and the Francevillian Group black shales (FB$_{1b-c}$ units, and FC and FD formations). Similarly, different scavenging capabilities of planktonic (in the Francevillian Group black shales) and benthic (in MRS) organic matter is not likely to explain weak enrichment in CE in the pyritized MRS. Rather, low CE/S ratios recorded by the pyritized MRS could be related to profuse sulfide production in pore-waters in microenvironments with high content of easily degradable benthic organic matter. Basinal restriction from the global ocean could have also diminished the reservoirs of metals and metalloids, which could have resulted in low CE/S ratios in the pyritized MRS. However, it is unlikely that the depletion of the basinal inventory of TE would have occurred at the time when the development of pyritized MRS took place, but not during deposition of the Francevillian Group black shales. Importantly, restricted basins with near-quantitative drawdown of the sulfate reservoir often show positive δ^{34}S values for early diagenetic pyrite (Diamond et al., 2018). By contrast, highly negative δ^{34}S values of the pyritized Francevillian Group macrobiota specimens point to bacterial sulfate reduction during early diagenesis with open connection to the overlying water column (El Albani et al., 2019, 2010). In this regard, we suggest that the amount of CE delivered to the sediments was largely controlled by both the mat thickness and sedimentary flux of organic matter (Figs. 9b, c). With high concentration of biogenic H$_2$S in the studied MRS, CE were not as enriched as in black shales from the Upper Francevillian Group, which were deposited under euxinic conditions where pyrite formed in the water column had ready access to a much larger reservoir of CE.

We propose that the pyrite formation and CE trapping in the pyritized MRS followed a two-stage process, resulting in weak enrichment in CE (Figs. 9b, c). First, the EPS degradation released to pore-waters CE, which were subsequently either incorporated into microcrystalline pyrite or returned to the water column (Fig. 9b). As EPS degradation takes place immediately after deposition (Decho et al., 2005), CE trapping at this stage was limited by sulfur and/or iron availability and, specifically, their reduction and release from the sediments. Hence, CE that were not trapped by pyrite diffused back to the water column, resulting in loss of co-variance between CE and S contents. During the second, protracted stage, most of remaining organic matter in sediments was degraded under anoxic and, locally, massive sulfidic conditions which resulted in the formation of coarse-grained, crystalline pyrite and overgrowths with low CE

contents (Fig. 9c). As this stage lasted longer, larger amounts of sulfide and iron were released to pore-waters, whereas pyrite formed was not enriched in CE since CE were either already trapped or lost from sediments during EPS degradation on the first stage.

The observed trend of weak enrichment in CE in the pyritized MRS thus reflects: (1) pyrite formation in pore-waters in the MRS and incorporation of CE delivered to the sediments with organic matter, specifically with EPS, and (2) the released to pore-waters during EPS degradation rather than a specific, biologically controlled pathway for accumulation of CE. Diagenetic pyrite production within the MRS likely also enhanced the potential for preservation of the Francevillian Group macrobiota.

5.4.   TE geochemistry: a biosignature of benthic microbial activity?

As discussed above, the TE content is greater in MRS than in host sediments of the FB_2 Member, a pattern that likely reflects variations in hydrodynamic regime and water-column redox chemistry. Specifically, the TE data for the Francevillian Group MRS suggest that the relationship between CE and sulfide concentrations are not consistent with a biological control over metal enrichment. These observations differ from Sforna et al. (2017) who suggested biologically controlled accumulation of TE in organic-rich globules in modern microbialites was a consequence of specific metabolic pathways (Sforna et al., 2017). By contrast, our results are similar to Rico et al. (2020) who observed that living microbial mats from the Middle Island Sinkhole (located 23 m below the water level of Lake Huron) do not significantly influence bulk TE geochemistry at the sediment–water interface, although highly heterogeneous redox conditions were observed. Considering that the water column redox conditions (*e.g.*, oxygen, sulfate, and iron concentrations) in the Middle Island Sinkhole could be analogous to those that were in Proterozoic shallow-marine environments (cf. Biddanda et al., 2012; Rico and Sheldon, 2019; Ruberg et al., 2008), we believe that these microbial mats provide a close analogue to the MRS of the Francevillian Group FB_2 Member. Together, TE data from benthic microbial communities in modern and ancient settings indicate that TE geochemistry is not a straightforward biosignature to be utilized in studies of the geological rock record.

6. Conclusion

Textural relationship and combined with TE geochemistry suggest distinct biological signals in the Francevillian Group MRS relative to their host sediments. However, no conclusive example of biologically controlled TE enrichment was found. Instead, our results, summarized in Figure 9, indicate highly variable TE contents with environmental factors overprinting biologically controlled TE distribution.

A lack of accumulation of heavy minerals and pyrite-hosted CE characterizes the EST. The poorly pyritized MRS contain in a high abundance of Ti- and Zr-bearing minerals concentrated through passive absorption. External morphology of these two MRS could be a potential biogenicity indicator and provides information on local environmental and ecological conditions, largely controlled by hydrodynamic regime and sediment supply. The CE concentrations in the poorly pyritized MRS co-vary ($R_2 = 0.85$) with pyrite content, which suggests that the CE are largely hosted by pyrite. Abundant organic matter in the now pyritized MRS did not result in similar CE/S ratios as in the Francevillian Group black shales deposited in euxinic settings due to the limited trapping capacity of pore-waters close to the sediment-water interface immediately after sediment deposition when CE-enriched EPS degraded. Arsenic-rich pyrite cores indicate high As concentrations in the early diagenetic pore-waters, where it was likely supplied via decay of EPS.

In summary, bulk-rock TE data provide additional evidence for biological activity during deposition of the *ca.* 2.1 Ga Francevillian Group, but there is no definitive biological signal since physical controls and water column redox chemistry outweighed microbial influences on the TE distribution in MRS. Recognition of the overprinting power of physical and chemical environmental conditions over microbially imprinted TE patterns in MRS further contributes to our understanding of interaction among ancient microbial life and the environmental and biological controls affecting TE contents in MRS, and their relationship to TE sinks in deep time.

Data availability. The authors declare that the data supporting this study are available within the paper and its supplementary information files.

Declaration of competing interests. The authors declare no competing interests.

References

Algeo, T.J., Tribovillard, N., 2009. Environmental analysis of paleoceanographic systems based on molybdenum–uranium covariation. Chemical Geology 268, 211–225. https://doi.org/10.1016/j.chemgeo.2009.09.001

Allwood, A.C., Walter, M.R., Kamber, B.S., Marshall, C.P., Burch, I.W., 2006. Stromatolite reef from the Early Archaean era of Australia. Nature 441, 714–718. https://doi.org/10.1038/nature04764

Amard, B., Bertrand-Sarfati, J., 1997. Microfossils in 2000 Ma old cherty stromatolites of the Franceville Group, Gabon. Precambrian Research 81, 197–221. https://doi.org/10.1016/S0301-9268(96)00035-6

Aubineau, J., El Albani, A., Bekker, A., Somogyi, A., Bankole, O.M., Macchiarelli, R., Meunier, A., Riboulleau, A., Reynaud, J.-Y., Konhauser, K.O., 2019. Microbially induced potassium enrichment in Paleoproterozoic shales and implications for reverse weathering on early Earth. Nat Commun 10, 2670. https://doi.org/10.1038/s41467-019-10620-3

Aubineau, J., El Albani, A., Chi Fru, E., Gingras, M., Batonneau, Y., Buatois, L.A., Geffroy, C., Labanowski, J., Laforest, C., Lemée, L., Mángano, M.G., Meunier, A., Pierson-Wickmann, A.-C., Recourt, P., Riboulleau, A., Trentesaux, A., Konhauser, K.O., 2018. Unusual microbial mat-related structural diversity 2.1 billion years ago and implications for the Francevillian biota. Geobiology 16, 476–497. https://doi.org/10.1111/gbi.12296

Azziley Azzibrouck, G., 1986. Sédimentologie et géochimie du Francevillien B (protérozoïque inférieur). Métallogénie des gisements de manganèse de Moanda, Gabon. Université Louis Pasteur, Strasbourg.

Bankole, O.M., El Albani, A., Meunier, A., Gauthier-Lafaye, F., 2015. Textural and paleo-fluid flow control on diagenesis in the Paleoproterozoic Franceville Basin, South Eastern, Gabon. Precambrian Research 268, 115–134. https://doi.org/10.1016/j.precamres.2015.07.008

Battin, T.J., Kaplan, L.A., Newbold, J.D., Cheng, X., Hansen, C., 2003. Effects of current velocity on the nascent architecture of stream microbial biofilms. Applied and Environmental Microbiology 69, 5443–5452. https://doi.org/10.1128/AEM.69.9.5443-5452.2003

Bekker, A., 2015a. Great Oxygenation Event, in: Gargaud, M., Irvine, W.M., Amils, R., Cleaves II, H.J., Pinti, D.L., Quintanilla, J.C., Rouan, D., Spohn, T., Tirard, S., Viso, M. (Eds.), Encyclopedia of Astrobiology. Springer-Verlag, Berlin, Heidelberg, pp. 1009–1017.

Bekker, A., 2015b. Lomagundi carbon isotope excursion, in: Gargaud, M., Irvine, W.M., Amils, R., Cleaves II, H.J., Pinti, D.L., Quintanilla, J.C., Rouan, D., Spohn, T., Tirard, S., Viso, M. (Eds.), Encyclopedia of Astrobiology. Springer-Verlag, Berlin, Heidelberg, pp. 1399–1404.

Bertrand-Sarfati, J., Potin, B., 1994. Microfossiliferous cherty stromatolites in the 2000 Ma Franceville group, Gabon. Precambrian research 65, 341–356.

Biddanda, B.A., Nold, S.C., Dick, G.J., Kendall, S.T., Vail, J.H., Ruberg, S.A., Green, C.M., 2012. Rock, water, microbes: underwater sinkholes in Lake Huron are habitats for ancient microbial life. Nature Education Knowledge 3, 13.

Bolhar, R., Kamber, B.S., Moorbath, S., Fedo, C.M., Whitehouse, M.J., 2004. Characterisation of early Archaean chemical sediments by trace element signatures. Earth and Planetary Science Letters 222, 43–60. https://doi.org/10.1016/j.epsl.2004.02.016

Bose, S., Chafetz, H.S., 2009. Topographic control on distribution of modern microbially induced sedimentary structures (MISS): A case study from Texas coast. Sedimentary Geology 213, 136–149. https://doi.org/10.1016/j.sedgeo.2008.11.009

Bouton, P., Thiéblemont, D., Simo Ndounze, S., Goujou, J.C., Kassadou, A.B., Walemba, A., Boulingui, B., Ekhogha, H., Moussavou, M., Lambert, A., Roberts, D., Deschamps, Y., Préat, A., 2009. Carte géologique de la République du Gabon à 1/200 000, feuille Franceville - Boumango.

Brasier, M.D., Green, O.R., Jephcoat, A.P., Kleppe, A.K., Van Kranendonk, M.J., Lindsay, J.F., Steele, A., Grassineau, N.V., 2002. Questioning the evidence for Earth's oldest fossils. Nature 416, 76–81. https://doi.org/10.1038/416076a

Bros, R., Stille, P., Gauthier-Lafaye, F., Weber, F., Clauer, N., 1992. Sm-Nd isotopic dating of Proterozoic clay material: An example from the Francevillian sedimentary series, Gabon. Earth and Planetary Science Letters 113, 207–218.

Canfield, D.E., Ngombi-Pemba, L., Hammarlund, E.U., Bengtson, S., Chaussidon, M., Gauthier-Lafaye, F., Meunier, A., Riboulleau, A., Rollion-Bard, C., Rouxel, O., Asael, D., Pierson-Wickmann, A.-C., El Albani, A., 2013. Oxygen dynamics in the aftermath of the Great Oxidation of Earth's atmosphere. Proceedings of the National Academy of Sciences 110, 16736–16741. https://doi.org/10.1073/pnas.1315570110

Carignan, J., Hild, P., Mevelle, G., Morel, J., Yeghicheyan, D., 2001. Routine analyses of trace elements in geological samples using flow injection and low pressure on-line liquid chromatography coupled to ICP-MS: a study of geochemical reference materials BR, DR-N, UB-N, AN-G and GH. Geostandards Newsletter 25, 187–198. https://doi.org/10.1111/j.1751-908X.2001.tb00595.x

Chappaz, A., Lyons, T.W., Gregory, D.D., Reinhard, C.T., Gill, B.C., Li, C., Large, R.R., 2014. Does pyrite act as an important host for molybdenum in modern and ancient euxinic sediments? Geochimica et Cosmochimica Acta 126, 112–122. https://doi.org/10.1016/j.gca.2013.10.028

Chi Fru, E., Somogyi, A., El Albani, A., Medjoubi, K., Aubineau, J., Robbins, L.J., Lalonde, S.V., Konhauser, K.O., 2019. The rise of oxygen-driven arsenic cycling at *ca*. 2.48 Ga. Geology 47, 243–246. https://doi.org/10.1130/G45676.1

Decho, A.W., Visscher, P.T., Reid, R.P., 2005. Production and cycling of natural microbial exopolymers (EPS) within a marine stromatolite. Palaeogeography, Palaeoclimatology, Palaeoecology 219, 71–86. https://doi.org/10.1016/j.palaeo.2004.10.015

Diamond, C.W., Planavsky, N.J., Wang, C., Lyons, T.W., 2018. What the ~1.4 Ga Xiamaling Formation can and cannot tell us about the mid-Proterozoic ocean. Geobiology 16, 219–236. https://doi.org/10.1111/gbi.12282

Dodd, M.S., Papineau, D., Grenne, T., Slack, J.F., Rittner, M., Pirajno, F., O'Neil, J., Little, C.T.S., 2017. Evidence for early life in Earth's oldest hydrothermal vent precipitates. Nature 543, 60–64. https://doi.org/10.1038/nature21377

Dupraz, C., Reid, R.P., Braissant, O., Decho, A.W., Norman, R.S., Visscher, P.T., 2009. Processes of carbonate precipitation in modern microbial mats. Earth-Science Reviews 96, 141–162. https://doi.org/10.1016/j.earscirev.2008.10.005

Dupraz, C., Visscher, P.T., 2005. Microbial lithification in marine stromatolites and hypersaline mats. Trends in Microbiology 13, 429–438. https://doi.org/10.1016/j.tim.2005.07.008

El Albani, A., Bengtson, S., Canfield, D.E., Bekker, A., Macchiarelli, R., Mazurier, A., Hammarlund, E.U., Boulvais, P., Dupuy, J.-J., Fontaine, C., Fürsich, F.T., Gauthier-Lafaye, F., Janvier, P., Javaux, E., Ossa, F.O., Pierson-Wickmann, A.-C., Riboulleau, A., Sardini, P., Vachard, D., Whitehouse, M., Meunier, A., 2010. Large colonial organisms with coordinated growth in oxygenated environments 2.1 Gyr ago. Nature 466, 100–104. https://doi.org/10.1038/nature09166

El Albani, A., Bengtson, S., Canfield, D.E., Riboulleau, A., Rollion Bard, C., Macchiarelli, R., Ngombi Pemba, L., Hammarlund, E., Meunier, A., Moubiya Mouele, I., Benzerara,

K., Bernard, S., Boulvais, P., Chaussidon, M., Cesari, C., Fontaine, C., Chi-Fru, E., Garcia Ruiz, J.M., Gauthier-Lafaye, F., Mazurier, A., Pierson-Wickmann, A.C., Rouxel, O., Trentesaux, A., Vecoli, M., Versteegh, G.J.M., White, L., Whitehouse, M., Bekker, A., 2014. The 2.1 Ga old Francevillian biota: Biogenicity, taphonomy and biodiversity. PLoS ONE 9, e99438. https://doi.org/10.1371/journal.pone.0099438

El Albani, A., Mangano, M.G., Buatois, L.A., Bengtson, S., Riboulleau, A., Bekker, A., Konhauser, K., Lyons, T., Rollion-Bard, C., Bankole, O., Lekele Baghekema, S.G., Meunier, A., Trentesaux, A., Mazurier, A., Aubineau, J., Laforest, C., Fontaine, C., Recourt, P., Chi Fru, E., Macchiarelli, R., Reynaud, J.Y., Gauthier-Lafaye, F., Canfield, D.E., 2019. Organism motility in an oxygenated shallow-marine environment 2.1 billion years ago. Proceedings of the National Academy of Sciences 116, 3431–3436. https://doi.org/10.1073/pnas.1815721116

Evensen, N., Hamilton, P., O'Nions, R., 1978. Rare-earth abundances in chondritic meteorites. Geochimica et Cosmochimica Acta 42, 1199–1212.

Flemming, H.-C., Wingender, J., Szewzyk, U., Steinberg, P., Rice, S.A., Kjelleberg, S., 2016. Biofilms: An emergent form of bacterial life. Nature Reviews Microbiology 14, 563–575. https://doi.org/10.1038/nrmicro.2016.94

Gauthier-Lafaye, F., 1986. Les gisements d'uranium du Gabon et les réacteurs d'Oklo. Modèle métallogénique de gîtes à fortes teneurs du protérozoique inférieur. Université Louis Pasteur, Strasbourg.

Gauthier-Lafaye, F., Weber, F., 1989. The Francevillian (Lower Proterozoic) uranium ore deposits of Gabon. Economic Geology 84, 2267–2285.

Gerdes, G., Klenke, T., Noffke, N., 2000. Microbial signatures in peritidal siliciclastic sediments: A catalogue. Sedimentology 47, 279–308.

He, J., Hu, H., Qiu, W., Liu, J., Liu, M., Zhao, C., Shi, X., Xu, J., 2016. Community diversity and biofilm characteristic response to low temperature and low C/N ratio in a suspended carrier biofilm reactor. Desalination and Water Treatment 57, 22212–22222. https://doi.org/10.1080/19443994.2015.1121840

Hiebert, R.S., Bekker, A., Houlé, M.G., Rouxel, O.J., 2018. Depositional setting of the Late Archean Fe oxide- and sulfide-bearing chert and graphitic argillite in the Shaw Dome, Abitibi greenstone belt, Canada. Precambrian Research 311, 98–116. https://doi.org/10.1016/j.precamres.2018.04.004

Holland, H.D., 2002. Volcanic gases, black smokers, and the Great Oxidation Event. Geochimica et Cosmochimica Acta 66, 3811–3826.

Homann, M., Heubeck, C., Airo, A., Tice, M.M., 2015. Morphological adaptations of 3.22 Ga-old tufted microbial mats to Archean coastal habitats (Moodies Group, Barberton Greenstone Belt, South Africa). Precambrian Research 266, 47–64. https://doi.org/10.1016/j.precamres.2015.04.018

Horie, K., Hidaka, H., Gauthier-Lafaye, F., 2005. U-Pb geochronology and geochemistry of zircon from the Franceville series at Bidoudouma, Gabon. Presented at the 15th Annual Goldschmidt Conference, Moscow, United States.

Huerta-Diaz, M.A., Delgadillo-Hinojosa, F., Otero, X.L., Segovia-Zavala, J.A., Martin Hernandez-Ayon, J., Galindo-Bect, M.S., Amaro-Franco, E., 2011. Iron and trace metals in microbial mats and underlying sediments: Results from Guerrero Negro saltern, Baja California Sur, Mexico. Aquat Geochem 17, 603–628. https://doi.org/10.1007/s10498-011-9126-3

Huerta-Diaz, M.A., Delgadillo-Hinojosa, F., Siqueiros-Valencia, A., Valdivieso-Ojeda, J., Reimer, J.J., Segovia-Zavala, J.A., 2012. Millimeter-scale resolution of trace metal distributions in microbial mats from a hypersaline environment in Baja California, Mexico. Geobiology 10, 531–547. https://doi.org/10.1111/gbi.12008

740 Huerta-Diaz, M.A., Morse, J.W., 1992. Pyritization of trace metals in anoxic marine
741   sediments. Geochimica et Cosmochimica Acta 56, 2681–2702.
742   https://doi.org/10.1016/0016-7037(92)90353-K
743 Jahnert, R.J., Collins, L.B., 2012. Characteristics, distribution and morphogenesis of subtidal
744   microbial systems in Shark Bay, Australia. Marine Geology 303–306, 115–136.
745   https://doi.org/10.1016/j.margeo.2012.02.009
746 Karhu, J.A., Holland, H.D., 1996. Carbon isotopes and the rise of atmospheric oxygen.
747   Geology 24, 867–870. https://doi.org/10.1130/0091-
748   7613(1996)024<0867:CIATRO>2.3.CO;2
749 Konhauser, K.O., 1998. Diversity of bacterial iron mineralization. Earth-Science Reviews 43,
750   91–121. https://doi.org/10.1016/S0012-8252(97)00036-6
751 Konhauser, K.O., 1997. Bacterial iron biomineralisation in nature. FEMS Microbiology
752   Reviews 20, 315–326. https://doi.org/10.1111/j.1574-6976.1997.tb00317.x
753 Konhauser, K.O., Fisher, Q.J., Fyfe, W.S., Longstaffe, F.J., Powell, M.A., 1998. Authigenic
754   mineralization and detrital clay binding by freshwater biofilms: The Brahmani river,
755   India. Geomicrobiology Journal 15, 209–222.
756   https://doi.org/10.1080/01490459809378077
757 Large, R.R., Danyushevsky, L., Hollit, C., Maslennikov, V., Meffre, S., Gilbert, S., Bull, S.,
758   Scott, R., Emsbo, P., Thomas, H., Singh, B., Foster, J., 2009. Gold and trace element
759   zonation in pyrite using a laser imaging technique: Implications for the timing of gold in
760   orogenic and carlin-style sediment-hosted deposits. Economic Geology 104, 635–668.
761   https://doi.org/10.2113/gsecongeo.104.5.635
762 Large, R.R., Mukherjee, I., Zhukova, I., Corkrey, R., Stepanov, A., Danyushevsky, L.V.,
763   2018. Role of upper-most crustal composition in the evolution of the Precambrian ocean–
764   atmosphere system. Earth and Planetary Science Letters 487, 44–53.
765   https://doi.org/10.1016/j.epsl.2018.01.019
766 Lekele Baghekema, S.G., Lepot, K., Riboulleau, A., Fadel, A., Trentesaux, A., El Albani, A.,
767   2017. Nanoscale analysis of preservation of *ca*. 2.1 Ga old Francevillian microfossils,
768   Gabon. Precambrian Research 301, 1–18.
769   https://doi.org/10.1016/j.precamres.2017.08.024
770 Li, Y.H., Schoonmaker, J., 2003. Chemical composition and mineralogy of marine sediments,
771   in: Mackenzie, F.T. (Ed.), Treatise on Geochemistry, Vol. 7: Sediments, Diagenesis, and
772   Sedimentary Rocks. Elsevier, Oxford, pp. 1–35.
773 Lindsay, J.F., Brasier, M.D., McLoughlin, N., Green, O.R., Fogel, M., Steele, A., Mertzman,
774   S.A., 2005. The problem of deep carbon—An Archean paradox. Precambrian Research
775   143, 1–22. https://doi.org/10.1016/j.precamres.2005.09.003
776 Lydmark, P., Lind, M., Sörensson, F., Hermansson, M., 2006. Vertical distribution of
777   nitrifying populations in bacterial biofilms from a full-scale nitrifying trickling filter.
778   Environ Microbiol 8, 2036–2049. https://doi.org/10.1111/j.1462-2920.2006.01085.x
779 Martin, A.P., Condon, D.J., Prave, A.R., Lepland, A., 2013. A review of temporal constraints
780   for the Palaeoproterozoic large, positive carbonate carbon isotope excursion (the
781   Lomagundi–Jatuli Event). Earth-Science Reviews 127, 242–261.
782   https://doi.org/10.1016/j.earscirev.2013.10.006
783 McLennan, S.M., 2001. Relationships between the trace element composition of sedimentary
784   rocks and upper continental crust: Trace element composition and upper continental
785   crust. Geochemistry, Geophysics, Geosystems 2, 2000GC000109.
786   https://doi.org/10.1029/2000GC000109
787 McLennan, S.M., 1989. Rare earth elements in sedimentary rocks: Influence of provenance
788   and sedimentary processes. Reviews in Mineralogy and Geochemistry 21, 169–200.
789 Medjoubi, K., Leclercq, N., Langlois, F., Buteau, A., Lé, S., Poirier, S., Mercère, P., Sforna,

M.C., Kewish, C.M., Somogyi, A., 2013. Development of fast, simultaneous and multi-technique scanning hard X-ray microscopy at Synchrotron Soleil. Journal of Synchrotron Radiation 20, 293–299. https://doi.org/10.1107/S0909049512052119

Mojzsis, S.J., Arrhenius, G., McKeegan, K.D., Harrison, T.M., Nutman, A.P., Friend, C.R.L., 1996. Evidence for life on Earth before 3,800 million years ago. Nature 384, 55–59.

Mouélé, I.M., Dudoignon, P., El Albani, A., Meunier, A., Boulvais, P., Gauthier-Lafaye, F., Paquette, J.-L., Martin, H., Cuney, M., 2014. 2.9–1.9 Ga paleoalterations of Archean granitic basement of the Franceville basin (Gabon). Journal of African Earth Sciences 97, 244–260. https://doi.org/10.1016/j.jafrearsci.2014.04.027

Nachtegaal, M., Scheidegger, A.M., Dähn, R., Chateigner, D., Furrer, G., 2005. Immobilization of Ni by Al-modified montmorillonite: A novel uptake mechanism. Geochimica et Cosmochimica Acta 69, 4211–4225. https://doi.org/10.1016/j.gca.2005.04.013

Newman, S.A., Klepac-Ceraj, V., Mariotti, G., Pruss, S.B., Watson, N., Bosak, T., 2017. Experimental fossilization of mat-forming cyanobacteria in coarse-grained siliciclastic sediments. Geobiology 15, 484–498. https://doi.org/10.1111/gbi.12229

Newman, S.A., Mariotti, G., Pruss, S., Bosak, T., 2016. Insights into cyanobacterial fossilization in Ediacaran siliciclastic environments. Geology 44, 579–582. https://doi.org/10.1130/G37791.1

Nutman, A.P., Bennett, V.C., Friend, C.R.L., Van Kranendonk, M.J., Chivas, A.R., 2016. Rapid emergence of life shown by discovery of 3,700-million-year-old microbial structures. Nature 537, 535–538. https://doi.org/10.1038/nature19355

Okabe, S., Hiratia, K., Ozawa, Y., Watanabe, Y., 1996. Spatial microbial distributions of nitrifiers and heterotrophs in mixed-population biofilms. Biotechnology and Bioengineering 50, 24–35.

Ossa Ossa, F., Eickmann, B., Hofmann, A., Planavsky, N.J., Asael, D., Pambo, F., Bekker, A., 2018. Two-step deoxygenation at the end of the Paleoproterozoic Lomagundi Event. Earth and Planetary Science Letters 486, 70–83. https://doi.org/10.1016/j.epsl.2018.01.009

Pecoits, E., Gingras, M.K., Barley, M.E., Kappler, A., Posth, N.R., Konhauser, K.O., 2009. Petrography and geochemistry of the Dales Gorge banded iron formation: Paragenetic sequence, source and implications for palaeo-ocean chemistry. Precambrian Research 172, 163–187. https://doi.org/10.1016/j.precamres.2009.03.014

Petrash, D.A., Gingras, M.K., Lalonde, S.V., Orange, F., Pecoits, E., Konhauser, K.O., 2012. Dynamic controls on accretion and lithification of modern gypsum-dominated thrombolites, Los Roques, Venezuela. Sedimentary Geology 245–246, 29–47. https://doi.org/10.1016/j.sedgeo.2011.12.006

Petrash, D.A., Lalonde, S.V., González-Arismendi, G., Gordon, R.A., Méndez, J.A., Gingras, M.K., Konhauser, K.O., 2015. Can Mn–S redox cycling drive sedimentary dolomite formation? A hypothesis. Chemical Geology 404, 27–40. https://doi.org/10.1016/j.chemgeo.2015.03.017

Planavsky, N.J., Bekker, A., Rouxel, O.J., Kamber, B., Hofmann, A., Knudsen, A., Lyons, T.W., 2010. Rare earth element and yttrium compositions of Archean and Paleoproterozoic Fe formations revisited: New perspectives on the significance and mechanisms of deposition. Geochimica et Cosmochimica Acta 74, 6387–6405. https://doi.org/10.1016/j.gca.2010.07.021

Playter, T., Konhauser, K.O., Owttrim, G., Hodgson, C., Warchola, T., Mloszewska, A.M., Sutherland, B., Bekker, A., Zonneveld, J.-P., Pemberton, S.G., Gingras, M., 2017. Microbe-clay interactions as a mechanism for the preservation of organic matter and trace metal biosignatures in black shales. Chemical Geology 459, 75–90.

840   https://doi.org/10.1016/j.chemgeo.2017.04.007

841 Pombo, F., 2004. Conditions de formation des carbonates de manganèse protérozosoïques et
842   analyse minéralogique et géochimique des minerais à bioxydes de manganèse associés
843   dans le gisement de Moanda (Sud-Est, Gabon). Université de Bourgogne, Dijon.

844 Préat, A., Bouton, P., Thiéblemont, D., Prian, J.-P., Ndounze, S.S., Delpomdor, F., 2011.
845   Paleoproterozoic high δ13C dolomites from the Lastoursville and Franceville basins (SE
846   Gabon): Stratigraphic and synsedimentary subsidence implications. Precambrian
847   Research 189, 212–228. https://doi.org/10.1016/j.precamres.2011.05.013

848 R Core Team, 2018. A language and environment for statistical computing. Vienna, Austria.

849 Reyes, K., Gonzalez, N.I., Stewart, J., Ospino, F., Nguyen, D., Cho, D.T., Ghahremani, N.,
850   Spear, J.R., Johnson, H.A., 2013. Surface orientation affects the direction of cone growth
851   by *Leptolyngbya sp.* strain C1, a likely architect of coniform structures Octopus Spring
852   (Yellowstone National Park). Applied and Environmental Microbiology 79, 1302–1308.
853   https://doi.org/10.1128/AEM.03008-12

854 Reynaud, J.-Y., Trentesaux, A., El Albani, A., Aubineau, J., Ngombi-Pemba, L., Guiyeligou,
855   G., Bouton, P., Gauthier-Lafaye, F., Weber, F., 2017. Depositional setting of the 2.1 Ga
856   Francevillian macrobiota (Gabon): Rapid mud settling in a shallow basin swept by high-
857   density sand flows. Sedimentology 65, 670–701.

858 Rico, K.I., Sheldon, N.D., 2019. Nutrient and iron cycling in a modern analogue for the
859   redoxcline of a Proterozoic ocean shelf. Chemical Geology 511, 42–50.
860   https://doi.org/10.1016/j.chemgeo.2019.02.032

861 Rico, K.I., Sheldon, N.D., Kinsman-Costello, L.E., 2020. Associations between redox-
862   sensitive trace metals and microbial communities in a Proterozoic ocean analogue.
863   Geobiology. https://doi.org/10.1111/gbi.12388

864 Rosing, M.T., 1999. 13C depleted carbon microparticles in >3700-Ma sea-floor sedimentary
865   rocks from West Greenland. Science 283, 674–676.

866 Ruberg, S.A., Kendall, S.T., Biddanda, B.A., Black, T., Nold, S.C., Lusardi, W.R., Green, R.,
867   Casserley, T., Smith, E., Sanders, G.T., Lang, G.A., Constant, S.A., 2008. Observations
868   of the Middle Island Sinkhole in Lake Huron – A unique hydrogeologic and glacial
869   creation of 400 Million Years. Mar Technol Soc J 42, 12–21.
870   https://doi.org/10.4031/002533208787157633

871 Sancho-Tomás, M., Somogyi, A., Medjoubi, K., Bergamaschi, A., Visscher, P.T., Van
872   Driessche, A.E.S., Gérard, E., Farias, M.E., Contreras, M., Philippot, P., 2018.
873   Distribution, redox state and (bio)geochemical implications of arsenic in present day
874   microbialites of Laguna Brava, Salar de Atacama. Chemical Geology 490, 13–21.
875   https://doi.org/10.1016/j.chemgeo.2018.04.029

876 Sarkar, S., Banerjee, S., Samanta, P., Chakraborty, N., Chakraborty, P.P., Mukhopadhyay, S.,
877   Singh, A.K., 2014. Microbial mat records in siliciclastic rocks: Examples from four
878   Indian Proterozoic basins and their modern equivalents in Gulf of Cambay. Journal of
879   Asian Earth Sciences 91, 362–377. https://doi.org/10.1016/j.jseaes.2014.03.002

880 Sarkar, S., Bose, P., Samanta, P., Sengupta, P., Eriksson, P., 2008. Microbial mat mediated
881   structures in the Ediacaran Sonia Sandstone, Rajasthan, India, and their implications for
882   Proterozoic sedimentation. Precambrian Research 162, 248–263.
883   https://doi.org/10.1016/j.precamres.2007.07.019

884 Schidlowski, M., Appel, P.W.U., Eichmann, R., Junge, C.E., 1979. Carbon isotope
885   geochemistry of the 3.7 x 109-yr-old Isua sediments, West Greenland: Implications for
886   the Archaean carbon and oxygen cycles. Geochimica et Cosmochimica Acta 43, 189–
887   199.

888 Schmitt, R., Smith, R., Olehy, D., 1964. Rare-earth, yttrium and scandium abundances in
889   meteoritic and terrestrial matter—II. Geochimica et Cosmochimica Acta 28, 67–86.

890 Sforna, M.C., Daye, M., Philippot, P., Somogyi, A., van Zuilen, M.A., Medjoubi, K., Gérard,
891   E., Jamme, F., Dupraz, C., Braissant, O., Glunk, C., Visscher, P.T., 2017. Patterns of
892   metal distribution in hypersaline microbialites during early diagenesis: Implications for
893   the fossil record. Geobiology 15, 259–279. https://doi.org/10.1111/gbi.12218
894 Shepard, R.N., Sumner, D.Y., 2010. Undirected motility of filamentous cyanobacteria
895   produces reticulate mats: Motility produces reticulate mats. Geobiology 8, 179–190.
896   https://doi.org/10.1111/j.1472-4669.2010.00235.x
897 Somogyi, A., Medjoubi, K., Baranton, G., Le Roux, V., Ribbens, M., Polack, F., Philippot, P.,
898   Samama, J.-P., 2015. Optical design and multi-length-scale scanning spectro-microscopy
899   possibilities at the Nanoscopium beamline of Synchrotron Soleil. Journal of Synchrotron
900   Radiation 22, 1118–1129. https://doi.org/10.1107/S1600577515009364
901 Suarez, C., Piculell, M., Modin, O., Langenheder, S., Persson, F., Hermansson, M., 2019.
902   Thickness determines microbial community structure and function in nitrifying biofilms
903   via deterministic assembly. Scientific Reports 9, 5110. https://doi.org/10.1038/s41598-
904   019-41542-1
905 Taylor, S.R., McLennan, S.M., 2001. Chemical composition and element distribution in the
906   Earth's Crust, in: Roberts, A.M. (Ed.), Encyclopedia of Physical Science and
907   Technology. Academic Press, New York, pp. 697–719.
908 Taylor, S.R., McLennan, S.M., 1985. The continental crust: Its composition and evolution.
909   Blackwell Scientific Puplications, Oxford.
910 Thiéblemont, D., Bouton, P., Préat, A., Goujou, J.-C., Tegyey, M., Weber, F., Ebang Obiang,
911   M., Joron, J.L., Treuil, M., 2014. Transition from alkaline to calc-alkaline volcanism
912   during evolution of the Paleoproterozoic Francevillian basin of eastern Gabon (Western
913   Central Africa). Journal of African Earth Sciences 99, 215–227.
914   https://doi.org/10.1016/j.jafrearsci.2013.12.007
915 Thiéblemont, D., Castaing, C., Billa, M., Bouton, P., Préat, A., 2009. Notice explicative de la
916   carte géologique et des ressources minérales de la République gabonaise à 1/1,000,000.
917 Tribovillard, N., Algeo, T.J., Lyons, T., Riboulleau, A., 2006. Trace metals as paleoredox and
918   paleoproductivity proxies: An update. Chemical Geology 232, 12–32.
919   https://doi.org/10.1016/j.chemgeo.2006.02.012
920 Van Zuilen, M.A., Lepland, A., Arrhenius, G., 2002. Reassessing the evidence for the earliest
921   traces of life. Nature 418, 627–630. https://doi.org/10.1038/nature00934
922 Weber, F., 1968. Une série précambrienne du Gabon : le Francevillien. Sédimentologie,
923   géochimie, relations avec les gîtes minéraux associés. Université de Strasbourg,
924   Strasbourg.
925 Weber, F., Gauthier-Lafaye, F., Whitechurch, H., Ulrich, M., El Albani, A., 2016. The 2-Ga
926   Eburnean Orogeny in Gabon and the opening of the Francevillian intracratonic basins: A
927   review. Comptes Rendus Geoscience 348, 572–586.
928   https://doi.org/10.1016/j.crte.2016.07.003
929 Webster-Brown, J.G., Webster, K.S., 2007. Trace metals in cyanobacterial mats,
930   phytoplankton and sediments of the Lake Vanda region, Antarctica. Antarctic Science 19,
931   311–319. https://doi.org/10.1017/S0954102007000417
932

933   APPENDIX A: SUPPLEMENTARY DATA

934

935   **Trace element perspective into the *ca*. 2.1-billion-year-old shallow-marine microbial**
936   **mats from the Francevillian Group, Gabon**

937

938   Jérémie Aubineau[1]*, Abderrazak El Albani[1], Andrey Bekker[2, 3], Ernest Chi Fru[4], Andrea
939   Somogyi[5], Kadda Medjoubi[5], Armelle Riboulleau[6], Alain Meunier[1], & Kurt O. Konhauser[7]

940

941   [1]UMR 7285 CNRS IC2MP, University of Poitiers, Poitiers, France
942   [2]Department of Earth and Planetary Sciences, University of California, Riverside, CA, 92521,
943   USA
944   [3]Department of Geology, University of Johannesburg, Auckland Park 2006, South Africa
945   [4]Centre of Geobiology and Geochemistry, School of Earth and Ocean Sciences, College of
946   Physical Sciences and Engineering, Cardiff University, Cardiff CF10 3AT, Wales, UK
947   [5]Nanoscopium beamline Synchrotron Soleil, BP 48, Saint-Aubin, 91192 GIF-sur-Yvette,
948   France
949   [6]UMR 8187 CNRS LOG, University of Lille, ULCO, Villeneuve d'Ascq, France.
950   [7]Department of Earth and Atmospheric Sciences, University of Alberta, Edmonton, Alberta,
951   Canada.

952

953   *corresponding author: jeremie.aubineau@univ-poitiers.fr
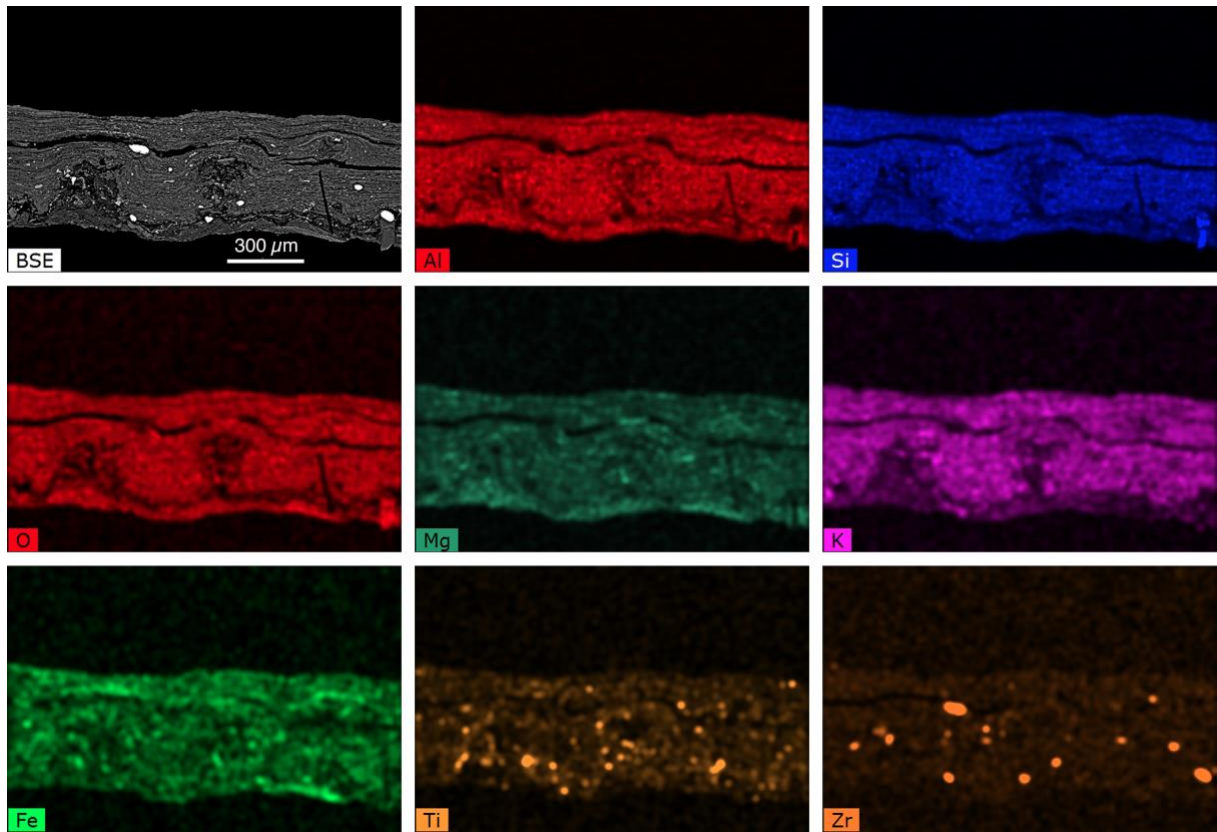
954

Figure S1. Petrography, SEM, and EDX of a poorly pyritized MRS in cross-section perpendicular to the bedding plane. Back-scattered electron (BSE) and composite (Al, Si, O, Mg, K, Fe, Ti, and Zr) elemental maps show mineral composition of the poorly pyritized MRS. A number of Ti- and Zr-rich heavy mineral grains are embedded within these mats.
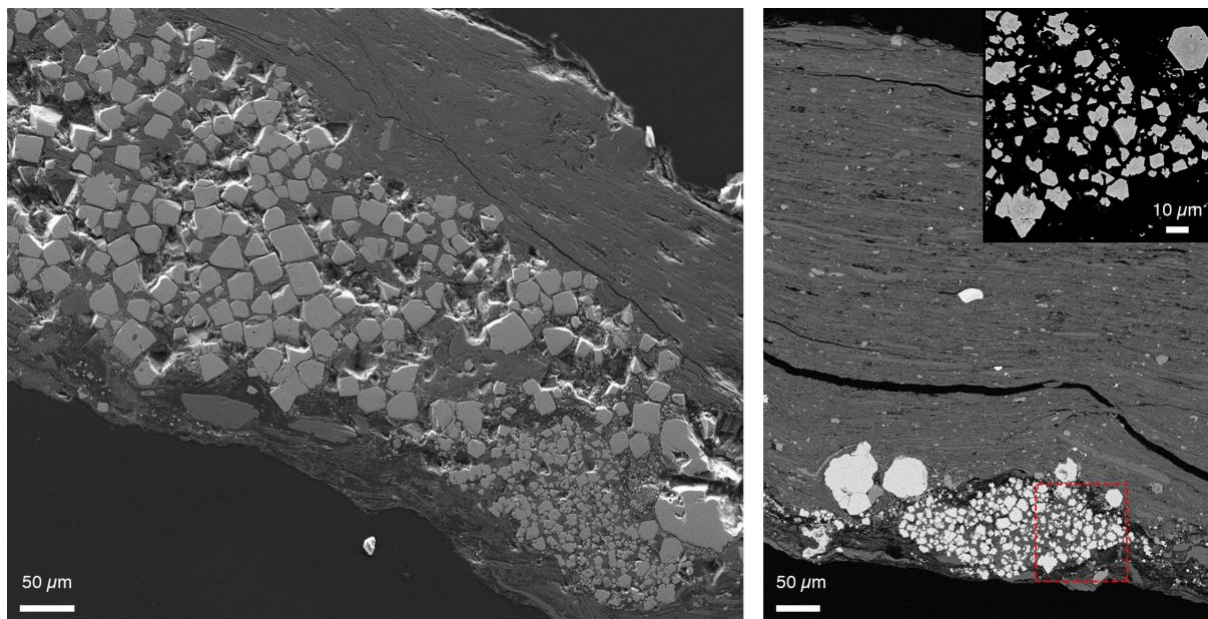
955

956

957

958

959

960

Figure S2. SEM image of poorly pyritized MRS in secondary electron (left) and BSE (right) modes. Pyrite-rich layers observed at the bottom of the MRS are highly variable in thickness. Inset shows numerous, tiny sub-euhedral to euhedral pyrite crystals.

966
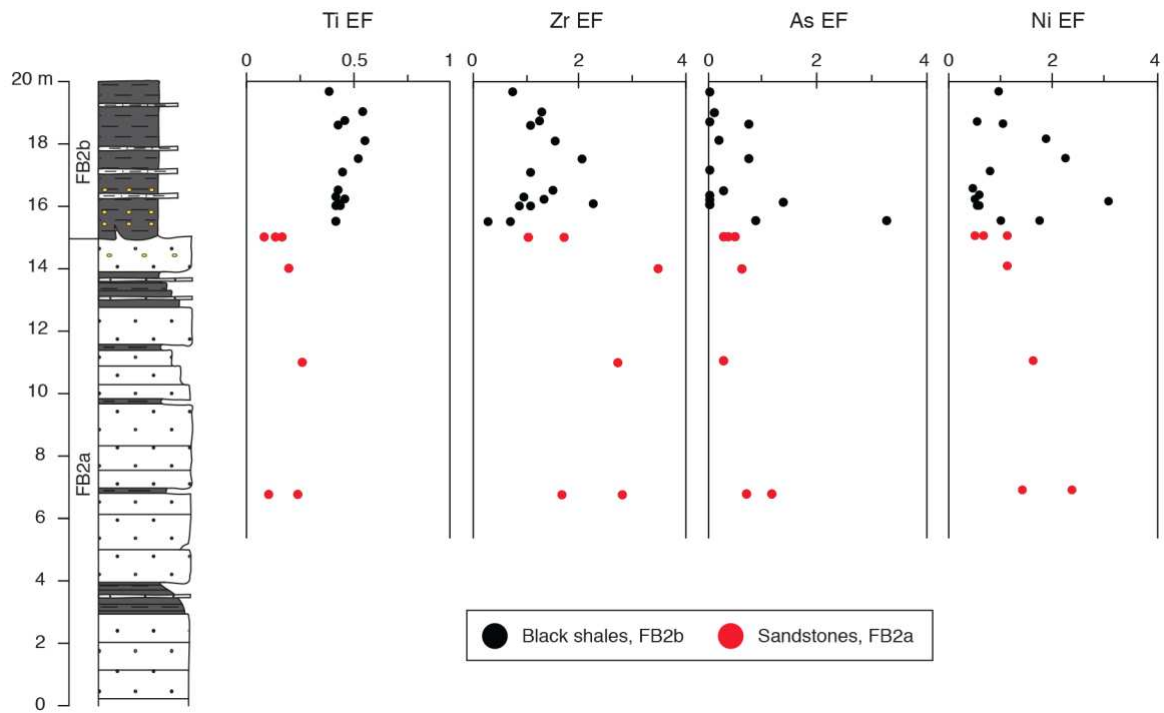
967 **Figure S3.** Stratigraphic profile with enrichment factor (EF) of selected immobile and
968 chalcophile elements within host sediments. EF are normalized to the average shale (Ti, Zr,
969 and Ni concentrations for the average shale are from Taylor and McLennan (2001), and As
970 concentration for the average shale is from Li and Schoonmaker, 2003).

971

972

TABLE S1. Whole-rock composition of major and trace elements and enrichment factors (EF)

of Ti, As, Ni, and Zr.

Formation	Lithology	Sample ID	Height m	Sr wt%	Si wt%	Al wt%	Fe wt%	Mn wt%	Mg wt%	Ca wt%	Na wt%	K wt%	Ti wt%	P wt%	EF$_{Ti}$	As ppm	Ba ppm	Bi ppm	Cd ppm
FB2b	Pyritized MRS	FPS_s5-mat	18.7	29.37	10.83	5.35	26.88	0.08	0.81	0.42	0.14	1.56	0.08	0.02	0.27	179.20	754.50	4.24	0.64
		DB_s4-mat	17.1	22.02	15.34	5.14	20.82	0.12	0.98	0.91	0.13	1.50	0.11	0.02	0.36	110.10	693.20	5.76	0.29
		FPS_s4-mat	16.3	24.81	9.91	4.37	29.04	0.07	1.09	0.58	0.10	1.11	0.07	0.02	0.28	111.90	526.50	4.01	0.21
		FPS_s3-mat	16.2	28.45	12.46	5.09	24.68	0.09	1.12	0.61	0.14	1.34	0.09	0.02	0.30	146.40	680.70	2.71	0.05
		DB_s2-mat	16.0	23.88	12.99	6.26	14.57	0.06	0.87	0.36	0.16	1.89	0.12	0.02	0.32	58.37	983.70	0.05	0.05
		DB_s3-mat	16.0	26.90	11.28	5.56	20.90	0.06	0.86	0.61	0.14	1.63	0.09	0.02	0.28	100.30	885.10	0.22	0.10
		FR_s1-mat	16.0	6.46	23.94	8.33	7.23	0.19	1.46	1.49	0.23	2.52	0.20	0.02	0.42	0.80	1234.00	0.25	0.57
	Black shales	WS_s1-sed	19.7	0.09	27.50	8.83	2.58	0.38	2.06	1.61	0.25	2.45	0.20	0.02	0.38	0.36	1131.81	0.11	0.23
		KS_s1-sed	19.0	0.09	28.86	8.02	2.67	0.18	1.81	1.48	0.22	2.35	0.25	0.09	0.53	1.41	1136.75	0.15	0.11
		FPS_s5-sed	18.7	0.22	26.30	8.85	1.67	0.37	1.82	1.89	0.25	2.63	0.23	0.07	0.45	0.80	1231.00	0.20	0.52
		AFBSO-12	18.6	N.D.	29.34	9.87	2.41	0.05	1.18	0.26	0.29	3.01	0.25	0.07	0.43	10.93	1505.00	0.31	0.34
		MLS_s7-sed	18.1	0.32	28.72	7.00	4.89	0.17	2.86	1.60	0.16	1.31	0.22	0.02	0.55	2.06	648.41	0.15	0.12
		AFBSO-9	17.5	N.D.	25.55	6.38	4.55	0.57	3.33	3.72	0.17	1.22	0.19	0.05	0.52	6.99	651.30	0.16	0.39
		DB_s4-sed	17.1	0.13	27.11	9.04	1.96	0.34	1.84	1.90	0.25	2.75	0.23	0.06	0.44	0.80	1294.00	0.21	0.42
		AFBSO-7	16.5	N.D.	36.25	7.03	0.25	0.01	0.32	0.01	0.16	2.36	0.17	0.06	0.42	2.94	1204.00	0.19	0.19
		FPS_s4-sed	16.3	0.16	30.88	6.37	6.21	0.09	1.85	0.17	0.16	1.12	0.16	0.07	0.41	0.80	1482.00	0.59	0.66
		FPS_s3-sed	16.2	0.17	26.98	9.85	1.54	0.20	1.64	1.48	0.26	3.10	0.24	0.07	0.46	0.80	1125.00	0.18	0.80
		AFBSO-6	16.1	N.D.	26.91	8.51	1.64	0.24	1.79	1.85	0.27	2.45	0.23	0.07	0.42	13.16	587.60	0.24	0.54
		DB_s2-sed	16.0	0.16	26.18	9.45	1.50	0.23	1.72	1.60	0.26	2.98	0.24	0.02	0.43	0.81	1318.60	0.09	0.15
		FR_s1-sed	16.0	0.20	27.21	9.98	1.65	0.19	1.86	1.55	0.28	3.14	0.24	0.06	0.41	0.80	1448.00	0.32	0.27
		MLS_s8-sed	15.5	1.02	25.34	10.97	2.71	0.37	1.86	1.50	0.29	3.57	0.27	0.02	0.41	53.11	1633.94	1.35	4.48
		MLS_s9-sed	15.5	0.34	26.27	10.13	2.12	0.28	1.80	1.50	0.27	3.21	0.25	0.02	0.42	13.23	1467.75	0.31	0.82
FB2a	Pyrite-poor MRS	MLS_s1-mat	15.0	4.16	15.75	11.96	9.17	0.25	2.48	0.72	0.26	3.46	1.66	0.24	2.39	50.84	1539.00	1.52	2.61
		LP_s3-mat	15.0	0.19	19.30	14.66	3.52	0.08	2.10	0.24	0.44	4.43	1.14	0.15	1.34	6.78	2035.00	0.86	0.65
		MLS_s2-mat	15.0	3.08	15.44	12.34	6.61	0.08	2.47	0.31	0.21	3.36	2.03	0.16	2.83	28.01	1409.00	2.33	3.35
		MLS_s6-mat	15.0	2.61	17.87	10.94	9.33	0.12	2.67	0.57	0.21	2.87	1.40	0.28	2.20	54.46	1225.00	1.43	1.84
		MLS_s4-mat	15.0	0.36	16.62	12.59	3.98	0.08	2.61	0.49	0.21	3.68	1.92	0.22	2.62	7.71	1512.00	1.39	2.54
		MLS_s5-mat	15.0	0.42	16.59	12.99	4.48	0.07	2.80	0.43	0.22	3.56	1.88	0.21	2.48	17.75	1488.00	1.64	2.59
		EST_s3-mat	15.0	0.36	14.78	14.76	2.43	0.03	3.37	0.02	0.29	2.31	0.22	0.04	0.26	2.33	1453.62	0.40	0.14
		EST_s4-mat	15.0	0.29	14.77	15.18	2.97	0.04	4.06	0.02	0.25	1.91	0.14	0.02	0.16	3.31	1203.89	0.28	0.12
		MLS_s3-mat	11.0	0.84	20.68	16.82	1.74	0.02	1.74	0.12	0.36	4.76	0.52	0.05	0.53	1.05	2542.63	0.41	0.11
		EST_s1-mat	6.9	0.17	16.93	16.41	1.90	0.01	3.34	0.07	0.37	2.96	0.20	0.02	0.21	1.56	2350.62	0.53	0.17
		EST_s2-mat	6.9	0.15	17.99	16.63	1.74	0.01	2.42	0.15	0.46	4.16	0.20	0.07	0.20	1.36	3253.14	0.34	0.16
	Sandstones	MLS_s1-sed	15.0	N.D.	41.65	2.47	0.68	0.09	0.58	0.47	0.08	0.50	0.02	0.02	0.13	1.90	281.40	0.18	0.27
		LP_s3-sed	15.0	N.D.	43.70	1.30	0.46	0.05	0.38	0.43	0.03	0.26	0.01	0.02	0.08	0.80	145.20	0.05	0.05
		MLS_s2-sed	15.0	N.D.	41.65	1.70	0.56	0.21	0.70	0.87	0.12	0.22	0.02	0.02	0.16	0.80	126.20	0.05	0.05
		LP_s2-sed	14.0	N.D.	44.35	1.10	0.39	0.01	0.24	0.04	0.03	0.16	0.01	0.01	0.20	1.01	95.36	0.02	0.04
		MLS_s3-sed	11.0	N.D.	44.09	1.51	0.47	0.02	0.35	0.01	0.02	0.18	0.02	0.02	0.26	0.70	97.90	0.02	0.03
		EST_s1-sed	6.9	0.02	44.21	1.05	0.40	0.01	0.12	0.01	0.01	0.24	0.01	0.02	0.10	1.14	120.74	0.08	0.05
		EST_s2-sed	6.9	N.D.	44.79	0.78	0.44	0.01	0.10	0.05	0.02	0.15	0.01	0.03	0.24	1.35	82.64	0.02	0.05

TABLE S1. (*Cont.*)

Formation	Lithology	Sample ID	Height m	Co ppm	Cr ppm	Cs ppm	Cu ppm	Hf ppm	Mo ppm	Nb ppm	Ni ppm	Pb ppm	Rb ppm	Sb ppm	Sn ppm	Sr ppm	Ta ppm	Th ppm	U ppm	V ppm	W ppm	Zn ppm	Zr ppm	EF$_{As}$	EF$_{Ni}$	EF$_{Zr}$
FB2b	Pyritized MRS	FPS_s5-mat	18.7	252.90	2.50	5.23	147.70	0.63	11.40	1.64	738.80	71.47	59.72	10.67	0.75	36.32	0.13	4.24	0.29	30.19	0.75	41.13	22.46	22.68	23.71	0.21
		DB_s4-mat	17.1	326.20	10.95	4.63	192.10	2.51	19.81	2.39	589.20	91.26	56.99	10.87	0.75	43.15	0.22	6.03	0.62	30.27	0.75	37.07	99.72	14.50	19.68	0.95
		FPS_s4-mat	16.3	192.60	2.50	4.00	82.20	0.72	13.94	1.47	587.60	42.72	43.84	5.42	0.75	27.62	0.11	3.70	0.30	23.48	0.75	61.04	25.64	17.32	23.07	0.29
		FPS_s3-mat	16.2	144.20	2.50	4.55	99.99	1.29	10.23	1.86	547.30	56.43	52.71	6.89	0.75	36.36	0.14	4.64	0.36	30.67	1.15	63.17	49.17	19.46	18.45	0.47
		DB_s2-mat	16.0	133.30	21.85	6.70	77.00	0.72	9.91	2.30	368.90	28.65	76.15	7.08	0.75	41.59	0.17	6.11	0.45	36.07	1.15	40.57	25.10	6.31	10.11	0.20
		DB_s3-mat	16.0	99.42	15.13	5.72	25.61	0.68	16.62	1.89	176.60	30.65	65.29	12.19	2.09	38.52	0.14	4.80	0.52	34.78	1.83	69.46	26.27	12.21	5.45	0.23
		FR_s1-mat	16.0	4.71	19.19	9.14	105.90	4.88	0.25	4.70	32.91	16.57	98.64	0.53	0.75	79.14	0.46	11.63	1.10	41.72	0.75	72.17	185.10	0.07	0.68	1.09
	Black shales	WS_s1-sed	19.7	5.35	37.00	7.95	40.13	3.53	0.25	4.14	48.88	5.11	95.17	0.19	0.75	74.20	0.38	10.03	0.83	43.01	1.31	102.44	134.81	0.03	0.95	0.75
		KS_s1-sed	19.0	6.67	41.72	9.00	56.13	5.56	0.25	5.65	52.08	8.45	105.30	0.30	1.23	94.24	0.52	15.96	1.32	38.73	2.08	82.31	210.10	0.12	1.12	1.29
		FPS_s5-sed	18.7	4.17	31.64	9.38	53.10	5.86	0.25	5.27	29.01	9.13	105.10	0.24	1.88	87.64	0.48	13.05	1.32	48.28	0.75	67.10	225.30	0.06	0.56	1.25
		AFBSO-12	18.6	8.89	54.76	11.08	56.63	5.58	0.76	5.91	60.68	10.77	125.30	0.54	1.28	86.32	0.53	14.44	1.21	52.97	1.66	93.85	220.00	0.75	1.06	1.09
		MLS_s7-sed	18.1	12.89	36.20	5.30	44.05	5.62	0.25	4.50	75.97	8.15	54.66	0.29	2.74	47.97	0.37	8.87	0.91	36.45	1.28	97.86	218.98	0.20	1.86	1.53
		AFBSO-9	17.5	20.14	40.61	5.53	34.59	6.76	0.76	4.61	83.16	13.44	53.93	0.83	1.31	69.97	0.42	10.76	1.08	32.39	1.01	150.50	265.40	0.74	2.24	2.04
		DB_s4-sed	17.1	4.18	36.33	8.54	58.04	5.07	0.25	5.63	42.64	15.05	108.40	0.26	1.94	91.59	0.53	13.53	1.24	49.54	1.78	65.61	197.00	0.06	0.81	1.07
		AFBSO-7	16.5	0.91	42.50	6.04	5.06	5.23	0.63	4.06	19.49	9.71	95.81	0.47	1.48	71.00	0.31	8.01	1.03	34.45	0.74	36.97	214.30	0.28	0.48	1.50
		FPS_s4-sed	16.3	5.06	33.76	10.73	51.88	5.03	0.25	5.53	33.91	12.30	126.10	0.28	1.63	85.90	0.47	13.54	1.25	49.99	1.71	53.87	192.20	0.05	0.59	0.96
		FPS_s3-sed	16.2	3.94	29.61	8.60	62.10	5.90	0.25	5.13	26.18	9.36	95.79	0.24	1.79	85.56	0.46	12.02	1.28	45.40	0.75	62.27	230.40	0.06	0.53	1.33
		AFBSO-6	16.1	49.92	30.15	4.40	28.16	7.20	0.85	3.56	115.10	34.22	47.05	1.38	0.99	49.69	0.35	9.47	1.02	29.13	0.88	168.90	293.30	1.40	3.10	2.26
		DB_s2-sed	16.0	3.43	47.73	10.63	57.57	5.48	0.72	5.28	30.55	5.42	119.66	0.27	0.75	85.09	0.50	14.45	1.32	57.54	1.60	65.24	208.76	0.06	0.56	1.08
		FR_s1-sed	16.0	5.30	33.21	11.02	57.01	4.65	0.25	5.33	33.45	18.15	123.80	0.25	4.15	83.97	0.47	12.81	1.24	50.73	1.64	54.19	179.90	0.05	0.58	0.88
		MLS_s8-sed	15.5	38.29	49.15	11.87	18.82	1.88	3.30	5.36	112.60	21.31	140.49	2.28	0.75	88.26	0.41	12.84	1.11	54.38	1.81	1475.71	66.57	3.28	1.76	0.30
		MLS_s9-sed	15.5	12.75	48.28	10.64	62.95	3.91	0.93	5.23	58.74	10.02	127.31	0.69	0.75	88.95	0.46	13.62	1.13	49.27	1.81	319.37	148.48	0.88	1.00	0.62
FB2a	Pyrite-poor MRS	MLS_s1-mat	15.0	45.86	196.00	12.28	208.60	45.66	4.76	39.34	228.80	97.64	148.20	7.95	9.40	294.90	3.71	77.88	8.54	96.43	8.75	306.10	1695.00	2.88	3.29	6.95
		LP_s3-mat	15.0	5.15	173.60	22.82	32.71	14.80	0.84	26.71	65.71	31.89	190.80	1.35	6.70	246.30	2.34	54.05	5.02	106.90	6.90	74.51	525.50	0.31	0.77	1.76
		MLS_s2-mat	15.0	48.40	230.40	11.76	155.50	79.20	3.66	47.91	223.90	72.37	145.10	5.47	4.56	322.60	4.35	111.20	10.16	91.74	9.52	194.70	2899.00	1.54	3.12	11.53
		MLS_s6-mat	15.0	32.23	149.30	11.57	115.40	44.86	4.63	31.62	167.30	96.24	124.40	7.36	3.14	242.80	2.99	64.95	8.28	84.62	7.03	144.10	1730.00	3.37	2.63	7.76
		MLS_s4-mat	15.0	15.79	208.40	13.32	121.10	57.13	1.44	44.54	134.20	33.47	166.90	1.47	3.45	346.00	4.05	99.45	8.92	93.92	8.69	179.80	2067.00	0.41	1.83	8.05
		MLS_s5-mat	15.0	13.24	193.70	13.09	64.23	65.04	2.29	43.48	119.40	42.29	155.20	2.50	3.50	321.10	4.09	96.85	9.20	99.93	8.43	112.90	2301.00	0.92	1.58	8.69
		EST_s3-mat	15.0	4.59	50.23	3.03	12.89	25.53	0.85	4.82	75.91	9.39	92.43	0.20	0.59	93.51	0.48	15.57	3.19	82.74	2.06	70.79	818.99	0.11	0.88	2.72
		EST_s4-mat	15.0	5.38	42.71	2.44	13.58	19.38	0.63	3.07	102.11	7.45	78.61	0.23	0.91	67.70	0.29	10.11	2.42	76.15	1.13	82.36	626.53	0.15	1.15	2.02
		MLS_s3-mat	11.0	5.83	87.81	17.74	21.95	16.57	0.25	11.74	69.91	19.58	193.92	0.32	2.31	206.52	1.04	27.29	2.92	77.14	1.83	45.30	523.94	0.04	0.71	1.53
		EST_s1-mat	6.9	2.50	36.93	4.14	8.04	25.87	0.25	4.52	133.24	2.86	110.63	0.21	0.23	105.07	0.41	16.59	3.95	78.76	1.38	77.22	996.31	0.06	1.39	2.98
		EST_s2-mat	6.9	1.76	36.63	5.10	7.41	25.89	0.57	4.59	94.95	2.68	175.82	0.17	3.50	136.12	0.43	16.73	3.51	75.49	2.01	61.00	832.59	0.06	0.98	2.46
	Sandstones	MLS_s1-sed	15.0	2.70	2.50	0.63	9.88	1.28	0.25	0.38	16.04	10.70	18.50	0.23	1.62	17.68	0.04	1.07	0.21	9.04	0.75	34.23	51.43	0.52	1.12	1.02
		LP_s3-sed	15.0	1.45	2.50	0.42	2.50	0.69	0.25	0.19	5.00	5.53	10.07	0.14	0.75	13.51	0.02	0.72	0.16	4.88	0.75	5.00	28.12	0.39	0.66	1.06
		MLS_s2-sed	15.0	1.71	2.50	0.41	2.50	1.46	0.25	0.43	5.00	4.39	8.70	0.15	0.75	14.86	0.04	1.01	0.20	6.23	0.75	17.75	58.75	0.30	0.50	1.69
		LP_s2-sed	14.0	0.73	3.92	0.42	1.00	1.94	0.25	0.28	7.42	2.56	6.71	0.13	0.48	9.35	0.03	0.64	0.20	4.36	0.40	14.90	77.72	0.62	1.15	3.46
		MLS_s3-sed	11.0	1.39	5.57	0.46	8.58	2.09	0.25	0.48	14.37	2.23	7.61	0.09	0.32	11.66	0.05	1.73	0.27	4.93	0.40	20.28	83.77	0.31	1.63	2.72
		EST_s1-sed	6.9	0.49	3.53	0.34	2.50	0.86	0.25	0.26	8.80	1.00	9.75	0.08	0.75	7.55	0.03	0.75	0.21	3.38	0.75	11.52	36.25	1.17	1.43	1.69
		EST_s2-sed	6.9	0.50	9.62	0.18	8.45	1.15	0.80	0.23	10.78	1.21	6.29	0.08	4.12	7.88	0.02	0.80	0.34	2.64	0.40	19.78	44.70	0.73	2.37	2.81

978   *Note*: FPS: flat, pyritized structure; DB: domal buildup; FR: "fairy-ring" structure; WS: wrinkle

979   structure; KS: "Kinneyia" structure; MLS: mat-layer structure; LP: linear pattern; EST:

980   "elephant-skin" texture as previously described by Aubineau et al. (2018).

981   EF_X refers to enrichment factor of X, where X stands for any chemical element.

982   Italicized numbers refer to samples for which half or more of the data were below the detection

983   limit. The detection limit is calculated as 6 times the standard deviation of the mean, plus the

984   mean, on 100 blank measurements.

985   N.D. = not determined.

986

987

988

TABLE S2. Bulk-rock data of rare earth elements and calculated Eu anomaly and REE
ratios.

Formation	Lithology	Sample ID	Height m	La ppm	Ce ppm	Pr ppm	Nd ppm	Sm ppm	Eu ppm	Gd ppm	Tb ppm	Dy ppm	Y ppm	Ho ppm	Er ppm	Tm ppm	Yb ppm	Lu ppm	∑LREE ppm	∑HREE ppm	REE_T ppm	Eu/Eu*	Y/Ho	Pr/Yb(SN)
FB2b	Pyritized MRS	FPS_s5-mat	18.7	11.12	20.43	2.13	7.49	1.22	0.26	0.86	0.12	0.52	2.43	0.10	0.23	0.03	0.17	0.03	42.39	2.06	44.70	1.24	25.32	3.95
		DB_s4-mat	17.1	17.24	32.25	3.46	12.30	2.11	0.47	1.48	0.20	1.06	4.22	0.20	0.53	0.08	0.48	0.08	67.35	4.09	71.90	1.30	29.85	2.33
		FPS_s4-mat	16.3	10.18	18.99	2.08	7.33	1.22	0.31	0.95	0.13	0.62	3.32	0.10	0.26	0.03	0.19	0.03	39.80	2.31	42.40	1.45	31.88	3.50
		FPS_s3-mat	16.2	13.32	24.70	2.64	9.06	1.47	0.35	1.09	0.14	0.74	5.97	0.13	0.35	0.05	0.28	0.04	51.20	2.84	54.40	1.36	31.51	2.98
		DB_s2-mat	16.0	16.46	30.21	3.24	11.21	1.84	0.42	1.41	0.16	0.85	4.52	0.15	0.35	N.D.	0.26	0.04	62.96	3.22	66.60	1.34	30.74	3.99
		DB_s3-mat	16.0	12.41	23.10	2.47	8.88	1.45	0.33	1.05	0.13	0.70	3.69	0.12	0.29	0.04	0.21	0.03	48.32	2.57	51.20	1.32	29.97	3.72
		FR_s1-mat	16.0	37.40	69.36	7.49	26.24	4.18	0.96	2.99	0.38	2.09	11.64	0.38	1.04	0.14	0.86	0.13	144.66	8.00	153.62	1.35	30.79	2.80
FB2b	Black shales	WS_s1-sed	19.7	30.05	56.98	6.24	22.18	3.61	0.84	2.60	0.33	1.78	10.18	0.34	0.86	0.11	0.73	0.11	119.05	6.86	126.80	1.36	30.33	2.74
		KS_s1-sed	19.0	52.75	97.05	10.26	35.49	5.39	1.21	3.65	0.45	2.46	13.85	0.47	1.21	0.17	1.08	0.16	200.94	9.64	211.80	1.35	29.69	3.05
		FPS_s5-sed	18.7	39.58	73.77	7.87	27.58	4.35	1.00	3.14	0.41	2.24	13.77	0.44	1.14	0.16	1.03	0.16	153.15	8.71	162.90	1.34	31.66	2.46
		AFBSO-12	18.6	43.37	80.44	8.70	30.55	4.91	1.08	3.51	0.45	2.44	14.30	0.43	1.20	0.16	1.06	0.16	167.96	9.41	178.50	1.29	33.41	2.63
		MLS_s7-sed	18.1	20.48	39.44	4.40	16.17	2.99	0.78	2.48	0.35	1.95	11.33	0.37	0.96	0.13	0.85	0.13	83.48	7.22	91.50	1.43	30.56	1.65
		AFBSO-9	17.5	23.51	44.25	4.91	18.16	3.22	0.83	2.57	0.37	2.12	13.78	0.40	1.14	0.16	1.09	0.17	94.05	8.01	102.90	1.41	34.45	1.45
		DB_s4-sed	17.1	39.38	73.87	8.02	28.10	4.47	1.00	3.22	0.39	2.17	12.84	0.41	1.09	0.15	0.98	0.16	153.84	8.58	163.40	1.32	31.09	2.62
		AFBSO-7	16.5	27.01	49.66	5.41	18.96	3.31	0.76	2.56	0.32	1.70	9.27	0.30	0.77	0.11	0.68	0.11	104.34	6.54	111.60	1.33	31.32	2.56
		FPS_s4-sed	16.3	40.15	74.22	8.04	27.99	4.64	1.03	3.37	0.43	2.34	13.58	0.43	1.12	0.15	1.00	0.15	155.04	9.00	165.10	1.30	31.44	2.58
		FPS_s3-sed	16.2	37.06	69.54	7.44	26.13	4.24	0.95	3.07	0.41	2.26	14.28	0.44	1.16	0.16	1.05	0.16	144.41	8.71	154.10	1.30	32.75	2.28
		AFBSO-6	16.1	27.14	51.97	5.69	20.58	3.71	0.95	2.88	0.39	2.16	13.20	0.40	1.09	0.16	1.04	0.16	109.09	8.28	118.30	1.44	33.33	1.76
		DB_s2-sed	16.0	41.91	76.86	8.24	28.54	4.52	1.03	3.20	0.41	2.32	14.26	0.45	1.19	0.16	1.08	0.16	160.07	8.96	170.10	1.34	31.68	2.46
		FR_s1-sed	16.0	40.05	74.26	8.07	27.95	4.72	1.05	3.39	0.41	2.17	12.78	0.42	1.06	0.14	0.93	0.14	155.05	8.66	164.80	1.32	30.43	2.79
		MLS_s8-sed	15.5	35.87	66.23	7.15	25.40	4.20	0.98	3.09	0.39	1.96	10.50	0.35	0.85	0.10	0.65	0.09	138.85	7.49	147.30	1.36	29.75	3.54
		MLS_s9-sed	15.5	39.22	72.68	7.82	27.62	4.46	1.02	3.19	0.40	2.15	12.25	0.40	1.04	0.14	0.88	0.13	151.81	8.33	161.20	1.35	30.40	2.85
FB2a	Pyrite-poor MRS	MLS_s1-mat	15.0	218.10	361.10	36.33	116.60	14.65	3.34	10.14	1.28	7.32	55.41	1.60	4.73	0.71	4.98	0.82	746.78	31.57	781.70	1.35	34.57	2.34
		LP_s3-mat	15.0	178.30	295.10	28.95	89.42	10.95	2.29	7.01	0.81	4.54	30.12	0.94	2.78	0.42	2.86	0.44	602.72	19.79	624.80	1.29	32.18	3.25
		MLS_s2-mat	15.0	292.10	498.70	53.00	184.50	16.83	3.12	9.92	1.38	8.62	62.18	1.95	6.25	1.02	7.10	1.17	1045.13	37.40	1085.60	1.12	31.85	2.39
		MLS_s6-mat	15.0	194.80	329.80	33.87	111.10	13.91	3.12	9.54	1.19	7.06	51.49	1.50	4.36	0.67	4.61	0.74	683.48	29.68	716.30	1.33	34.30	2.35
		MLS_s4-mat	15.0	302.70	507.50	52.35	170.40	17.08	3.41	10.91	1.38	8.19	58.78	1.78	5.54	0.87	6.11	1.00	1050.03	35.78	1089.20	1.21	33.08	2.75
		MLS_s5-mat	15.0	278.90	460.60	47.22	156.80	16.58	3.32	10.27	1.31	8.00	59.31	1.74	5.50	0.89	6.31	1.04	960.10	35.05	998.50	1.22	34.18	2.40
		EST_s3-mat	15.0	30.56	55.73	5.93	21.94	4.00	1.10	2.83	0.41	2.78	22.20	0.64	1.89	0.29	2.09	0.34	118.16	11.27	130.50	1.57	34.76	0.91
		EST_s4-mat	15.0	18.50	34.40	3.86	14.81	2.73	0.76	2.21	0.35	2.34	19.02	0.53	1.52	0.23	1.56	0.25	74.31	8.97	84.00	1.48	36.01	0.79
		MLS_s3-mat	11.0	79.32	140.17	15.25	54.45	9.10	2.20	6.73	0.82	4.18	20.62	0.75	1.90	0.28	1.96	0.30	298.29	16.93	317.40	1.42	27.46	2.49
		EST_s1-mat	6.9	21.06	39.22	4.40	17.14	3.32	0.86	2.25	0.36	2.47	20.09	0.58	1.84	0.29	2.14	0.35	85.14	10.28	96.30	1.45	34.38	0.66
		EST_s2-mat	6.9	19.36	36.11	4.07	16.25	3.39	0.87	2.56	0.39	2.50	17.93	0.56	1.63	0.26	1.87	0.31	79.17	10.07	90.10	1.42	31.93	0.70
FB2a	Sandstones	MLS_s1-sed	15.0	3.65	7.52	0.92	3.92	1.02	0.33	0.99	0.13	0.73	4.54	0.13	0.30	0.03	0.20	0.03	17.03	2.54	19.90	1.73	34.38	1.48
		LP_s3-sed	15.0	2.48	5.54	0.72	3.16	0.74	0.22	0.70	0.09	0.48	2.75	0.09	0.19	0.02	0.12	0.02	12.63	1.70	14.50	1.60	30.88	1.87
		MLS_s2-sed	15.0	3.53	7.01	0.81	3.20	0.71	0.18	0.59	0.08	0.44	2.82	0.09	0.22	0.03	0.18	0.03	15.26	1.66	17.10	1.43	31.30	1.40
		LP_s2-sed	14.0	1.93	4.23	0.42	1.67	0.35	0.11	0.32	0.05	0.27	1.93	0.06	0.15	0.02	0.16	0.03	8.60	1.05	9.80	1.60	33.79	0.86
		MLS_s3-sed	11.0	3.27	6.41	0.76	2.92	0.55	0.14	0.43	0.06	0.32	2.08	0.06	0.18	0.03	0.19	0.03	13.91	1.30	15.40	1.45	33.35	1.29
		EST_s1-sed	6.8	2.09	4.28	0.48	1.76	0.44	0.13	0.48	0.07	0.37	2.08	0.07	0.15	0.02	0.12	0.02	9.05	1.29	10.50	1.43	30.93	1.31
		EST_s2-sed	6.9	1.76	3.54	0.40	1.53	0.39	0.11	0.42	0.06	0.38	2.21	0.08	0.18	0.03	0.16	0.02	7.62	1.33	9.10	1.42	29.46	0.80

1004 **TABLE S3.** Weight of each principal component.

1005

	eigenvalue	variance %	cumulative variance %
PC1	14.12	54.32	54.32
PC2	6.35	24.44	78.76
PC3	1.87	7.18	85.94
PC4	1.36	5.22	91.15
PC5	0.73	2.82	93.98
PC6	0.47	1.8	95.78
PC7	0.34	1.32	97.1
PC8	0.24	0.92	98.02
PC9	0.15	0.58	98.6
PC10	0.11	0.43	99.04
PC11	0.09	0.33	99.37
PC12	0.05	0.17	99.54
PC13	0.03	0.13	99.68
PC14	0.02	0.09	99.77
PC15	0.02	0.07	99.84
PC16	0.01	0.06	99.9
PC17	0.01	0.04	99.94
PC18	0.01	0.02	99.96
PC19	0	0.01	99.98
PC20	0	0.01	99.99
PC21	0	0.01	99.99
PC22	0	0	100
PC23	0	0	100
PC24	0	0	100
PC25	0	0	100
PC26	0	0	100

1006

1007